ICARUS 116, 77–112 (1995)

The Near-Nucleus Coma Formed by Interacting Dusty Gas Jets Effusing from a Cometary Nucleus: I

J. F. CRIFO

Service d'Aéronomie du CNRS, B.P.3, F91371 Verrières-le-Buisson Cedex, France
E-mail: crifo©aerov.jussieu.fr

A. L. ITKIN AND A. V. RODIONOV

International Institute for Problems of the Asteroid Hazard, Bol. Kommunisticheskaya Ul., 25 Moscow, 109004, Russia

Received June 22, 1994; revised February 7, 1995

The first step of a development of a multipurpose numerical code for the realistic simulation of the circumnuclear coma of an active comet is described. First, the basic equations and numerical integration method are described; the adequacy of the method is demonstrated by a new computation of the interaction between two identical dusty water jets as treated in Y. Kitamura (1990, *Icarus* 86, 455–475). The general characteristics of the previous results are reproduced, but with a greater numerical accuracy; more importantly, we show that the two-fluid approach used there is invalid and must be replaced by a three-fluid approach. Second, we compute the structure of a coma formed from three identical jets, using a four-fluid approximation. Third, we introduce physical parameters more suitable for a comparison with P/Halley flyby results, and we compute the structure of a single-jet, a two-jets, and a three-jets coma. The results confirm that the relation between coma structure and dusty gas production geometry is not simple. In particular, the formation of radial dust density enhancements *away from* the vertical of the active regions is usually predicted, which implies that the brightness patterns of the near-nucleus dust coma are *not necessarily* easy-to-interpret tracers of the nucleus active region pattern. The limits of the present results are discussed, and the future steps of development of the model are indicated. © 1995 Academic Press, Inc.

1. INTRODUCTION

Eight years after Comet P/Halley flyby missions, the essential questions that one currently raises concerning comets remain without satisfactory answers. The composition and morphology of the nucleus of a comet are essentially unknown, as well as its pattern of emission. We do not have a single data point concerning the atmosphere that surrounds it (or "coma") at *less than* 500 km from its surface (distance at which the Comet Halley flyby observations stopped); neither do we have any fully interpreted neutral mass spectrum of any coma. There is very incomplete information on the size distribution of cometary dust and on its chemical nature and no information at all on dust grain shapes. Finally, there exist no direct measurement of dust velocities; so the present estimates of cometary mass losses (i.e., of active regions composition and lifetime) are untrustworthy (Crifo 1988).

For such and other reasons, the European Space Agency has decided to implement the long-duration rendez-vous mission "Rosetta" to a comet. This mission, to be realized during the first decade of the 21st century, is focused on the observation of the least understood, but most significant regions of a comet, viz. the solid nucleus and its immediate environment.

It is a real challenge to optimize a single-mission program for the study of media which are nearly unknown. The risk of missing essential measurements exists only for the reason that they were not anticipated to be essential. For instance, in our opinion one of the reasons that the 1986 flyby missions to P/Halley did not carry instruments to detect heavy dust was the widespread but poorly founded belief that comets emit dominantly small grains (see Crifo 1988). The Rosetta primary observational targets, the nucleus and circumnuclear coma, are practically *not* accessible to direct observations. Thus, efforts dedicated to their simulation by laboratory experiments or numerical simulations seem appropriate.

While sophisticated efforts have been made to model the outer coma, and its interaction with the solar wind, only a few significant studies have been devoted hitherto to the circumnuclear coma. Almost all of these were performed assuming a crude representation of the nucleus, of the emitted dust (if any), and of the emitted gas (see Crifo 1991, Gombosi 1991).

This paper presents the *first step* of development of a computer code dedicated to the realistic simulation of the immediate vicinity of an active comet nucleus. In its *final*

0019-1035/95 $12.00
Copyright © 1995 by Academic Press, Inc.
All rights of reproduction in any form reserved.

form, the model will (1) treat the nucleus as a rotating irregularly shaped object (viz. an irregular polyhedron), with an uneven pattern of gas and dust emission; (2) treat the dust as a natural substance, i.e., exhibiting a broad dispersion in size and shape; and (3) model the water flow with allowance for its well-established physicochemical properties. Such an objective can be met only through a succession of upgrading steps, starting from the present sophistication level; separate presentations of the partial achievements of the program need also to be made, in order to make clear the physical significance of the final, very complex, model. Furthermore, we conjecture that not all the properties of the coma are affected by all the processes that govern the outflow of gas and dust: with the present approach, it will be possible to identify which level of sophistication is indeed needed for simulating any specific property of the inner coma.

The main goal of the present first phase of our work is to validate the specially developed numerical method that will be used in the model. The validation consists essentially of duplicating the results of Kitamura (1990) where the interaction of two identical dusty gas jets issuing from two identical spots located close to one another on a spherical nucleus surface was investigated. This work, which we will in the following designate by the acronym K90, was selected because it is the only three-dimensional, shock-capturing, dusty-gas cometary model published to this date. For optimizing such a comparison, we deliberately did not change any physical assumption made in K90. As currently occurs when computations are duplicated, we have indeed reproduced part of the results of K90, thereby validating our method, but, in addition, we have also identified some deficiencies in K90. We discuss these deficiencies in detail, since one of them helps to point out (for the first time) eventual improper uses of the multifluid approach.

Using again the same set of physical parameters, we have computed the interaction between *three* identical dusty gas jets in a symmetrical configuration: by comparing with the two-jets case, a deeper understanding of the physical process which leads to the formation of a real circumnuclear coma is possible.

Kitamura's parameters are not optimal for a comparison with P/Halley's flyby data. Therefore, we have found of interest to recompute two-jet and three-jet coma structures using a new choice of parameters more suitable for such a purpose. We have also computed a single-jet solution (using the new set of parameters) to completely clarify the physical process of gas and dust pattern production.

The present results confirm that, as was first realized by Kitamura, the interactions between dusty gas jets issuing from several areas of a nucleus surface will form "narrow features of the gas and small-size dust, which have a *jet-like structure*" (K90, page 471): accordingly, the fine dust patterns in the inner coma *are not* trivial tracers of the active area distribution. We indicate why such a conclusion is not expected to be invalidated by the incorporation of a more satisfactory gas and dust representation. This is a consequential conclusion: it implies that reliable interpretations of Comet P/Halley near-nucleus images (Keller *et al.* 1987), as well as reliable identification of nucleus active regions from the future Rosetta observations, should *not* be based on simple, intuitive concepts of the formation of the circumnuclear coma.

2. GOVERNING EQUATIONS

It is possible to make sufficiently reliable inferences on the composition of the circumnuclear coma: H_2O has been identified as the dominant species in the outer coma of Comet P/Halley, and there is all indication that such is the case for most comets; owing to its chemical stability, H_2O must dominate as well in the innermost coma; fine dust is always present in the outer coma, therefore also in the inner one. Heavy dust is present also, and though poorly known, bounds on its possible abundance are such that it should not greatly affect the inner coma gas flow. A wealth of minor chemical species, such as C-bearing, N-bearing, and S-bearing compounds, is very probably present in the region: however, their incorporation in our model was not considered essential (even though there are various other reasons that one might be willing to consider at least one non-water-group molecule, e.g., CO or CH_3OH) because, due to their small abundance, these species cannot influence much the global structure of the region. Thus, in its initial steps of development, our model assumes that the region is formed by multiphase outflow under deep rarefaction and solar illumination of a dust–H_2O mixture.

The main gas species, H_2O, is the best conceivable example of a condensible vapor that is also a triatomic molecule which is an efficient infrared emitter. Pure water underexpanded outflow is thus from the outset very diabatic, but here, in addition, one must allow for the coupling with dust. At some distance from the surface, the coma becomes transparent to UV solar light, which triggers a gas-phase photochemistry which, again, affects the flow.

2.1. *Physical Model*

The question of which governing equations are appropriate for a medium in which particles with widely differing mass coexist is a delicate one, in particular when a fast rarefaction of the medium can prevent the attain-

ment of mutual equilibrium between some, or all, of the constituents.

Here, we have chosen to make use of the multifluid approximation Crifo (1991), whereby it is implied that the interaction between identical constituents is much more efficient than that between differing ones. It is essential to note that, as the details of the solution are not a priori known, the validity of this approach must be justified a posteriori on the basis of the results.

2.1.1. The H_2O fluid. It is well known that a pure fluid expanding in a vacuum evolves across a succession of regimes, e.g., fluid regime, transition regime, and free-molecular outflow. However, our purpose is to model a region with size not much exceeding 10 nucleus sizes; therefore, only one flow regime only will be normally encountered. For the present conditions, the H_2O initial mean free path (mfp) is of the order of 20 cm, and the characteristic active region dimension is 1 km, so that the gas flow in the vicinity of the active region is inviscid: Euler equations are a priori suitable. We discuss this point further below.

Another well-known fact is that if the fluid particles have internal degrees of freedom, equilibrium may cease to prevail between them and the fluid translational components, due to the speed of the expansion. Here, as in K90, the rotational and vibrational disequilibrium of the H_2O molecule (Crovisier 1984) is accounted for by the crude approximation of adopting a constant ratio of specific heats $\gamma = 4/3$ (in other words, the rotational levels are assumed to be in local thermal equilibrium, and the vibrational modes are thought to be unexcited).

2.1.2. The dust fluid(s). As in K90, we *initially* use a two-fluid model: separate hydrodynamic equations are written for the gas (fluid 1) and for the single-size, single-shape dust grains (fluid 2).

As far as dust (considered as a fluid) is concerned, the discussion of the flow equations requires an assessment of its initial velocity, which sets its initial density and thus its collision rate. This is impossible, because we do not know for sure the dust release process at the surface. Therefore, for the sake of simplicity, as did previous authors, we assume that mutual collisions between dust grains are absent. It can be verified by the solution that such is indeed the case at the distance from the surface where the model becomes physically significant ($\simeq$10 m). Accordingly the "dust fluid" has zero *internal* pressure and zero *kinetic* temperature. (Another, perhaps more satisfactory interpretation may be given to the zero-temperature assumption: even if some mutual collisions between dust grains occur, the coupling with the gas is so strong that the former does not affect the dust dynamics significantly.)

Introducing such a concept, however, raises strong difficulties.

First, one violates the basic requirement of the multifluid approximation, i.e., *that collisions between similar particles be dominant.* Indeed, as was shown in Rodionov (1995) and as discussed here in Section 5, the simple-minded procedure of treating single-size dust as a single zero-temperature fluid is not applicable to the present problem and has led to spurious results in K90. It is nonetheless possible to treat this problem and related ones by a multifluid method, but the number of dust fluids to consider may be large and must be carefully conjectured a priori and verified a posteriori.

Second, the use of a fluid approach sets constraints on the fluid element size: the collisions *within* any fluid element, which give a physical meaning to the summations over the conservative quantities (mass, momentum, and energy), must be frequent enough. Thus the dimensions of the fluid element must exceed the fluid mfp. At zero temperature, the latter is infinite. One may, however, interpret, in this case, the macroscopic dust fluid quantities as trivial sums over noninteracting particles *that share common dynamical parameters*. This, in turn, requires that the fluid element size exceeds *the mean interparticle distance* (m.i.d.). Again, these conditions must be checked a posteriori (Section 5).

2.2. Gas Dynamics Equations

In contrast with earlier works, Cartesian coordinates are used, since one of our future goals is to put an end to the use of a spherical (or any other symmetrically structured) nucleus surface.

Even though in the following only time-stationary solutions are presented, time-dependent equations are described here for two reasons: (i) In the immediate vicinity of the nucleus surface, where the sonic point is crossed and shock structures are expected to form, the steady-state solution is defined as the limit for infinite times of a time-dependent solution computed from simple initial conditions (this method was introduced by Gombosi (1985) and also was used in Kitamura (1990)). (ii) In the future, we will take into account real time-dependent effects, e.g., allow for the nucleus rotation and transient activity.

The time-dependent inviscid (Euler) equations, in conservative form, read

$$\frac{\partial \mathbf{U}}{\partial t} + \frac{\partial \mathbf{E}}{\partial x} + \frac{\partial \mathbf{F}}{\partial y} + \frac{\partial \mathbf{G}}{\partial z} = \mathbf{H}, \tag{2.1}$$

where

$$\mathbf{U} = \begin{vmatrix} \rho \\ \rho u \\ \rho v \\ \rho w \\ \rho h_0 - P \end{vmatrix}, \mathbf{E} = \begin{vmatrix} \rho u \\ \rho u^2 + P \\ \rho uv \\ \rho uw \\ \rho uh_0 \end{vmatrix}, \mathbf{F} = \begin{vmatrix} \rho v \\ \rho uv \\ \rho v^2 + P \\ \rho vw \\ \rho vh_0 \end{vmatrix}, \mathbf{G} = \begin{vmatrix} \rho w \\ \rho uw \\ \rho vw \\ \rho w^2 + P \\ \rho wh_0 \end{vmatrix}, \mathbf{H} = \begin{vmatrix} f_\rho \\ f_u \\ f_v \\ f_w \\ f_h \end{vmatrix}. \quad (2.2)$$

Here t is time, x, y, z are Cartesian coordinates, u, v, and w the corresponding components of velocity, ρ and P the density and static pressure of the gas, respectively, and $h_0 = h + (u^2 + v^2 + w^2)/2$ is the total enthalpy, where $h = \gamma P/(\gamma - 1)\rho$ is the specific enthalpy.

The source terms $f_\rho \ldots f_h$ represent the net mass, momentum, and energy budget of exchanges between gas and dust particles, of absorption and emission of IR radiation by the gas, and of photochemical reactions within the gas.

The temperature does not explicitly appear in Eq. (2.1). It can be obtained from the equation of state

$$P = \rho RT/\mathcal{M}, \quad (2.3)$$

where R is the universal gas constant and $\mathcal{M}$ the molecular weight of the gas.

2.3. Dust Dynamics Equations

Taking into account the zero-pressure approximation, the Euler equations for one "dust fluid" read

$$\frac{\partial \mathbf{U}_s}{\partial t} + \frac{\partial \mathbf{E}_s}{\partial x} + \frac{\partial \mathbf{F}_s}{\partial y} + \frac{\partial \mathbf{G}_s}{\partial z} = \mathbf{H}_s, \quad (2.4)$$

where

$$\mathbf{U}_s = \begin{vmatrix} \rho_s \\ \rho_s u_s \\ \rho_s v_s \\ \rho_s w_s \\ \rho_s e_s \end{vmatrix}, \mathbf{E}_s = \begin{vmatrix} \rho_s u_s \\ \rho_s u_s^2 \\ \rho_s u_s v_s \\ \rho_s u_s w_s \\ \rho_s u_s e_s \end{vmatrix}, \mathbf{F}_s = \begin{vmatrix} \rho_s v_s \\ \rho_s u_s v_s \\ \rho_s v_s^2 \\ \rho_s v_s w_s \\ \rho_s v_s e_s \end{vmatrix}, \mathbf{G}_s = \begin{vmatrix} \rho_s w_s \\ \rho_s u_s w_s \\ \rho_s v_s w_s \\ \rho_s w_s^2 \\ \rho_s w_s e_s \end{vmatrix}, \mathbf{H}_s = \begin{vmatrix} f_{s,\rho} \\ f_{s,u} \\ f_{s,v} \\ f_{s,w} \\ f_{s,e} \end{vmatrix}. \quad (2.5)$$

Here u_s, v_s, and w_s are the Cartesian components of the dust fluid flow velocity, ρ_s is the *mass* density of the dust fluid, $e_s = c_s T_s$ its specific internal energy, c_s its specific heat capacity, T_s its *internal* temperature, and the f_s source-sink terms which result from the interaction between dust and gas, from the dust IR emission, and from the absorption of solar radiation. Notice that, in a nonequilibrium medium, it is essential to distinguish internal temperature from kinetic temperature, this being true for dust grains as well as for gas molecules.

It may look surprising that there be the same number of unknowns for the gas and for the dust fluid, in spite of the fact that the latter has a known (zero) kinetic temperature: the reduction from six dynamical variables to five model unknowns is ensured for the gas by the equation of state and for the dust fluid by the equation "dust kinetic temperature = 0."

In the following, we will also present solutions in which there are two or three dust fluids; the governing equations are (2.1) and (2.4), but now the subscript s is to be understood as a label for the dust fluids; i.e., $s = 1, 2, \ldots$

3. MODEL PARAMETERS AND BOUNDARY CONDITIONS

The parameters of the model consist of a set of physical constants describing assumed nucleus properties, a set of algorithms for the terms f and f_s, and a set of boundary conditions for the $5(s + 1)$ variables.

For the first part of the present results, we have used exactly the same assumptions as in K90. For the remaining results, we have changed some of the parameters in order to bring the physical conditions closer to those prevailing in P/Halley at the time of the 1986 flybys.

The validity of these assumptions is discussed in Appendix A.

3.1. Source-Sink Algorithms

These algorithms allow the specification of the two right-hand-side (rhs) vectors $\mathbf{H}$ and $\mathbf{H}_s$. They represent the

effect of radiative processes (labeled by the superscript "rad"), of the gas-phase chemistry, and of the interphase (gas–dust, superscripts g and d) exchanges.

3.1.1. Radiative terms. The net radiative budget of the H_2O molecule is here taken to be zero: in other words, absorption and reemission of IR photons are assumed to balance one another. Kitamura has also produced solutions in which a nonzero IR radiative energy loss is introduced. We have not done this here.

As regards the dust grains, they are assumed to be spherical, and treated as gray absorbers with Mie (visible light) absorption efficiency $q_{\text{abs}} \equiv 1$, and gray radiators with emissivity $q_{\text{emit}} \equiv 0.41$. Introducing the solar flux $f_\odot$ and the Stefan–Boltzman constant σ, one has

$$f_{s,e}^{\text{rad}} = n_s \pi a_s^2 (q_{\text{abs}} f_\odot - 4\, q_{\text{em}} \sigma T_s^4) = \frac{3\rho_s}{4\tilde{\rho}_s a_s} (q_{\text{abs}} f_\odot - 4\, q_{\text{em}} \sigma T_s^4). \tag{3.1}$$

Here, the solar flux at 1 AU is used, n_s is the number density of the dust fluid, $\tilde{\rho}_s$ the specific mass of the dust material, a_s the dust radius.

Equation (3.1) does not include any diffuse radiation field nor optical thickness effect. In the immediate vicinity of a nucleus surface, however, visible and IR emission from the nucleus surface and partial extinction of the solar flux by the dust should have been taken into account. In our earlier 1-d works (e.g., Crifo 1992), this was done, and found to introduce only a small difference in the variation with distance to the surface of the dust temperature: therefore, the present approximation is acceptable.

3.1.2. Gas phase chemistry. In an expansion-cooled vapor (especially in the case of H_2O) a wealth of nucleation reactions leading to the formation of embryos of the condensed phases, currently take place. Furthermore, if the medium is transparent to UV light, gas phase photochemistry sets in. Here, the perturbations of the gas flow by these two effects is neglected. This is as in K90, except that, there, a constant "optically thin" (i.e., upper limit) photochemical heating rate was used; but it was found to play a negligible role on the solutions.

3.1.3. Gas–dust interaction. In first place, the dust is assumed to be "inert," whereby it does not contribute to the term f_ρ in Eq. (2.2), and $f_{s,\rho} \equiv 0$ in Eq. (2.5).

Next, in the present application, a_s is everywhere much smaller than the gas mfp, whereby the usual free-molecular expressions can be used for the contribution of the gas–dust interaction to the rhs terms in Eq. (2.4):

$$\mathbf{f}_s^{\text{g}} \equiv (f_{s,u}^{\text{g}}, f_{s,v}^{\text{g}}, f_{s,w}^{\text{g}}) = \frac{3}{8} \frac{\rho_s \rho}{a_s \tilde{\rho}_s} C_{\text{D}} |\mathbf{W} - \mathbf{W}_s| (\mathbf{W} - \mathbf{W}_s) \tag{3.2}$$

$$f_{s,e}^{\text{g}} = 3 \frac{\rho_s \rho}{a_s \tilde{\rho}_s} C_p \,\text{St}\, |\mathbf{W} - \mathbf{W}_s| (T_{\text{r}} - T_s). \tag{3.3}$$

Here $\mathbf{W} \equiv (u, v, w)$, $\mathbf{W}_s \equiv (u_s, v_s, w_s)$, C_p is the specific heat capacity of the gas ($C_p = h/T$), $C_{\text{D}} \equiv C_{\text{D}}(\omega, T_s/T)$ is the drag coefficient, $\text{St} \equiv \text{St}(\omega, \gamma)$ the Stanton number, $T_{\text{r}} \equiv T_{\text{r}}(T, \omega, \gamma)$ the grain recovery temperature, and $\omega = |\mathbf{W} - \mathbf{W}_s| / \sqrt{2P/\rho}$ the relative speed ratio. The classical expressions for C_{D}, St, and T_{r} are written down in K90.

In the present case where $f_{s,\rho} \equiv 0$, interphase momentum and energy conservation yields for the contribution of the dust–gas interaction to the rhs terms in Eq. (2.1)

$$\mathbf{f}^{\text{d}} \equiv (f_u^{\text{d}}, f_v^{\text{d}}, f_w^{\text{d}}) = -\mathbf{f}_s^{\text{g}} \tag{3.4}$$

$$f_h^{\text{d}} = -(f_{s,e}^{\text{g}} + \mathbf{W}_s \cdot \mathbf{f}_s^{\text{g}}). \tag{3.5}$$

Here we have corrected a mistake in K90 where the term $\mathbf{W} \cdot \mathbf{f}_s^{\text{g}}$ was written instead of the correct expression $\mathbf{W}_s \cdot \mathbf{f}_s^{\text{g}}$. Expression (3.5) is in complete agreement with Gombosi *et al.* (1985) and with Crifo (1991). Although for the problem considered $\mathbf{W}_s \neq \mathbf{W}$, our investigation shows that this correction has a very small effect on the results. This can be explained by the fact that *under the present conditions* the dust influence on the gas energy budget is due mainly to the term $f_{s,e}^{\text{g}}$.

When there is more than one dust fluid, Eqs. (3.2) and (3.3) hold for each fluid, and in the rhs of Eqs. (3.4) and (3.5) one must carry a summation over s.

3.1.4. Conclusion. For all results presented here, the vectors $\mathbf{H}$ and $\mathbf{H}_s$ are, respectively,

$$\mathbf{H} = (0, f_u^{\text{d}}, f_v^{\text{d}}, f_w^{\text{d}}, f_h^{\text{d}}); \quad \mathbf{H}_s = (0, f_{s,u}^{\text{g}}, f_{s,v}^{\text{g}}, f_{s,w}^{\text{g}}, f_{s,e}^{\text{g}} + f_{s,e}^{\text{rad}}). \tag{3.6}$$

3.2. Nucleus Physical Constants

Let us first note that, since our (and Kitamura's) computations are done only inside a limited domain, we need *not* specify completely the nucleus shape (we do not use the nucleus mass either because here we deal only with fine dust). We need to specify only the shape of the part of the nucleus surface *which lies within the computational domain*. Here, it is assumed to be a spherical rectangle cut from a sphere with radius $r_0 = 6$ km. Within this domain, the active areas of the nucleus surface consist of one, two, or three spherical squares with side δ, arranged in a symmetrical configuration (see Fig. 1). The number of squares and the value of δ for the various solutions computed here are given in Table I, together with the angular distance between the centers of the active areas, Δ.

The active areas of the nucleus emit water vapor at a *total* mass loss rate mQ g sec^{-1} (where m is the water

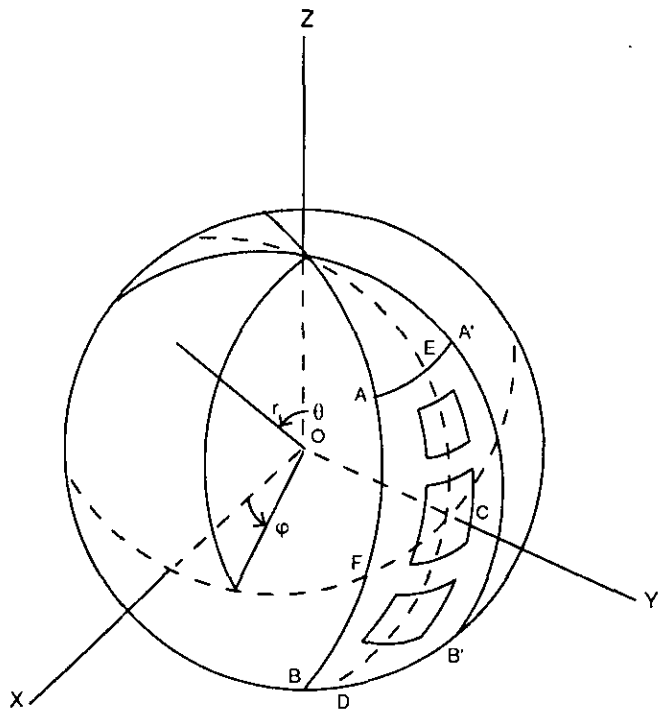

FIG. 1. Geometry of the problem. The case of three active regions is shown; for two regions, the central one is omitted; for one region the two side regions are omitted. The domain where the coma structure is computed extends outward from the spherical rectangle AA'BB'; outside of this rectangle, the nucleus shape need not be specified. The computational domain is the spherical rectangle AECF. The origin of coordinates is O and the Cartesian axes spherical angles are shown. The distance OC is equal to 6 km. All results are presented in the plane OECD.

molecule mass) and identical spherical dust grains with radius a_s, specific mass $\tilde{\rho}_s = 1.0$ g cm^{-3}, and specific heat $c_s = 6.0 \times 10^6$ erg g^{-1} K^{-1} at a *total* mass loss rate $m_s Q_s \equiv \chi mQ$ (where m_s is the dust grain mass and χ a free parameter). The values of a_s and χ differ from solution to solution and are given in Table I.

For optimal intercomparison of the results, it would have been best to adopt a few fixed values of Q. Here, this is not the case, in compliance with what was done in K90. One has

$$mQ = r_0^2 \int\int \rho_0(\theta, \phi) V_0(\theta, \phi) \sin\theta d\theta d\phi \equiv r_0^2 \langle \rho_0 V_0 \rangle \mathcal{A}, \tag{3.7}$$

where θ is the colatitude, ϕ the longitude, $\mathcal{A}$ the *total* active area size, the summation is carried over all active regions, and the subscript (0) labels the gas initial parameters. The values of Q corresponding to the present solutions range from $\simeq 3 \times 10^{28}$ sec^{-1} to $\simeq 6 \times 10^{29}$ sec^{-1}.

The heliocentric distance is given in K90 as equal to 1 AU; in fact, it enters into consideration only indirectly, via the f, f_s algorithms.

3.3. Boundary Conditions

They consist, first, in a set of values for the $5(s + 1)$ variables at the nucleus surface, both inside and outside of the active regions. Because the solutions are here looked for only within a closed domain (not over full space), artificial boundary conditions have also to be defined at the fictitious surfaces which enclose the computational domain.

In the present study, we look only for stationary solutions: all *initial* values of the flow variables are independent of time. Their numerical values are listed in Table II and are described in the following sections. Notice that the value of ρ_0 used here is such that $\rho_0 c_0 \simeq f_\odot / L_s$, where c_0 is the initial sound speed and L_s the ice latent heat of sublimation.

3.3.1. Surface boundary conditions. The initial velocity of the gas, $\mathbf{V}_0$ is taken to be radial *over the whole emitting surface*. For a pure gas jet (i.e., for $\chi = 0$) its value is taken to be equal to $c_0 \simeq 350$ m sec^{-1}. If dust is present, its value is determined by the special time-dependent procedure used in Kitamura (1986, 1987, 1990) and described in some detail in Appendix B. The resulting

TABLE I
Nucleus Parameters

Solution	δ (°)	$\mathcal{A}$ (km^2)	Δ (°)	mQ (kg sec^{-1})	Q (sec^{-1})	χ	a_s (μm)
2 Small jets	10	1.985	50	1.25×10^3	4.19×10^{28}	0.00	—
2 Small jets	10	1.985	50	8.14×10^2	2.72×10^{28}	0.20	0.1
2 Small jets	10	1.985	50	1.03×10^3	3.45×10^{28}	0.20	1.0
2 Small jets	10	2.116	30	8.68×10^2	2.90×10^{28}	0.20	0.1
3 Small jets	10	2.992	30	1.23×10^3	4.11×10^{28}	0.20	0.1
1 Large jet	50	26.55	—	1.67×10^4	5.60×10^{29}	0.02	10.
2 Large jets	36	24.69	56	1.56×10^4	5.21×10^{29}	0.02	10.
3 Large jets	30	23.56	45	1.48×10^4	4.97×10^{29}	0.02	10.

TABLE II
Initial Boundary Conditions at $r = r_0$

Variable	Symbol	Initial value(s) ($r = r_0$)
Gas temperature (K)	T_0	200
Gas specific mass (kg m^{-3})	ρ_0	1.8×10^{-6}
Gas velocity	V_0	See text
Dust temperature (K)	$T_{s,0}$	348
Dust velocity	$V_{s,0}$	See text
Dust *fluid* specific mass	$\rho_{s,0}$	$\chi\rho_0 V_0/V_{s,0}$

gas velocity varies with position within the active areas, but is approximately equal to $0.65c_0$ for Kitamura's values $\chi = 0.2$ and $a_s = 0.1$ μm; for $\chi = 0.2$ and $a_s = 1$ μm, it is approximately 0.83 c_0. It is nearly equal to c_0 for the solutions with $\chi = 0.02$.

Notice that, due to the dependence of V upon χ, the solutions dust-free and dusty, shown here and in K90, correspond to slightly different gas and dust production rates.

On the nucleus surface outside of the active spots, a slip-wall condition is applied: in other words, the dusty gas is assumed to flow parallel to the nucleus surface, without friction or heat exchange. Kitamura has also presented solutions for the case where there is a background source all over the surface; such cases which require no special numerical developments are not treated here.

3.3.2. Artificial boundary conditions. In all cases treated here, there are two planes of symmetry: $\theta = 90°$ and $\phi = 90°$. With this geometry, the solution of the problem is sought in the restricted region $r_0 < r < r_m$, $\theta_0 < \theta < 90°$, $\phi_0 < \phi < 90°$, where r_m is a limiting distance. The values adopted for θ_0 and ϕ_0 were chosen to ensure a comparable accuracy for all the solutions presented here and are given in Table III.

The following artificial boundary conditions are used at the limiting surfaces of the computational domain.

On the cone $\theta = \theta_0$, on the plane $\phi = \phi_0$, and on the spherical rectangle $r = r_m$ we apply free-outflow boundary conditions.

On the planes $\theta = 90°$ and $\phi = 90°$ the symmetry of the flow is used; this is at variance with K90, where the symmetry with respect to the plane of interaction ($\theta = 90°$) was not exploited, with the consequence that the dimension of his computational domain was twice greater than here.

4. NUMERICAL METHOD

The design constraints for the numerical method are the following: (1) it must accommodate a general tridimensional geometry (i.e., deprived from symmetry simplifications since the comet nucleus may assume any kind of complicated shape); (2) it must handle a priori unknown shocks resulting either from the interaction between distinct gas jets emitted at differing places on the nucleus surface K90 or from strong ("supercritical") latent heat release during the partial recondensation of H_2O (Delale *et al.* 1993, Schnerr 1993).

The basic numerical method used in this study is a second-order variant of Godunov's method specially developed to handle flows with strong discontinuities (for instance, shock waves) in a general way, i.e., without the need to prescribe a priori the localization of these discontinuities. It is described in detail in Rodionov (1987a,b, 1994). Appendix C gives a concise outline of the method, and Table III lists some computational parameters.

The region of the coma explored here extends from the nucleus surface $r = r_0$ up to a limiting distance r_m. In contrast with K90, this region is split into two subregions, $r_0 < r < r_1$ and $r_1 < r < r_m$, where different numerical methods are used.

In the inner region ($r_0 < r < r_1$), subsonic flow is susceptible to occur, first, in the region *between* the verticals of the active areas, where jets interact, and, second, if there is dust, in the immediate vicinity of the active areas. For that reason, the solution is here obtained with the help of a time asymptotic method, as in K90.

For ($r \geq r_1$), the flow is everywhere supersonic; therefore, the solution is obtained using a *steady* economical "marching" method, integrating upward from $r = r_1$ up to $r = r_m$. This allows a reduction in total computational time, with the computer time needed for the upper region becoming two orders of magnitude smaller than that for the lower one. This means that the computational resources do not depend much upon the value of r_m.

The choice of r_1 is of course not critical at all: it is chosen on the basis of a conjecture concerning the extent of the subsonic regions, conjecture which is checked a posteriori from inspection of the solution obtained.

All results presented here were computed with $r_0 = 6$ km and $r_m = 100$ km; the values of r_1 are given in Table III.

TABLE III
Computational Parameters

	r_1 (km)	$\Delta\theta$ (°)	$\Delta\phi$ (°)	J_1	θ_0 (°)	ϕ_0 (°)
2 Small jets (K90 case)	14	2.00	1.67	20	50	70
3 Small jets	8.2	1.67	1.25	10	30	75
1 Large jet	10	2.50	2.50	16	15	40
2 Large jets	11	2.00	2.00	16	2	54
3 Large jets	10	1.88	1.88	18	7.5	60

5. RESULTS

In the following, two different kinds of results are presented. First, the interaction of two jets is computed using exactly the assumptions of K90. Two variants of this solution (different grain size and different jet separation) are also offered; besides it, we compute the structure of a coma formed by three identical jets, using assumptions close to those of K90. Finally, since these assumptions are not ideally suited for comparison with P/Halley flyby results, we also show one-jet, two-jets, and three-jets solutions in which more satisfactory parameters (for such a purpose) are used. Table I indicates the nucleus parameters used in all solutions, and Table III lists the computational parameters.

5.1. Interaction between Two Identical Pure Gas Jets (Kitamura Case)

We first consider ejection from two active areas symmetrically located with respect to the Comet-to-Sun axis $\theta = \phi = 90°$. The first area is the spherical square $60° < \theta < 70°$, $85° < \phi < 95°$ (about 1 × 1-km edges); the second area is the spherical square $110° < \theta < 120°$, $85° < \phi < 90°$ (same size). Thus the angular distance between the centers of these active areas is equal to 50° (about 5 km).

We start by assuming that there is no dust at all ($\chi = 0$). In this case, the total water production rate is 4.19×10^{28} sec^{-1}. Figure 2 presents the gas isodensity contours. One notices that the results obtained in the first and in the second computational domains—respectively obtained by the time asymptotic approach and by the marching method—smoothly connect with one another at $r = r_1$.

As previous calculations have already shown (Rodionov 1994), there is a small *systematic* difference between the results obtained by the present method and those of K90: the presently computed gas densities are slightly, but systematically, smaller. This can be shown (Appendix D) to be a consequence of the fact that in K90 the computed points are at corners of the computational cells, while here they are at cell centers; one can compute that Kitamura's gas densities exceed the correct ones by the factor ≈1.4.

Otherwise, the interaction region obtained here is closely similar to that shown in Fig. 4(b) of K90: the most conspicuous features are, at low altitudes, the two standing, nearly plane shock waves that enclose shocked gas. Notice that these shock structures are, indeed, not exactly planes, but diverge from one another rather like in a horn. The shocked gas forms what could be called a "secondary" jet. The density enhancement in this secondary jet is about of a factor 3 at large distance, and greater closer to the surface. Notice that, carved in its middle, is a narrow gas density depression: its origin is well understood, but rather lengthy to explain; it will be sufficient, here, to say that it follows from a decrease in shock strength upward along the shock surfaces.

The apparition of such nonintuitive gas pattern in the coma clearly demonstrates the impossibility of tracing back gas density measurements to nucleus surface active areas without relevant hydrodynamic modeling.

In the nonshocked regions, the gas density decrease follows approximately a $(R/\hat{r})^2$ law, where R is the "effective radius" of the active area, and $\hat{r}$ the distance to a point situated at R below the surface on the active area axis. In other words, very close to the surface, the gas seems to come from a sphere with radius R, *not* r_0. This behavior was predicted in Crifo (1991) on general grounds and provides a justification for testing physical models of the coma in spherically symmetric geometry.

5.2. Interaction between Two Identical Dusty Gas Jets (Kitamura Case)

The preceding computations was repeated, but introducing dust grains with $a_s = 0.1$ μm and $\chi = 0.2$. The reduction in initial gas velocity results in a total gas production rate of 2.72×10^{28} sec^{-1}.

5.2.1. The need for a conservative formalism for the dust equations. The comparison of our computed dust distribution (Fig. 3) with that of K90 reveals a number of discrepancies.

First, it appears that Kitamura's dust number densities are everywhere (away from the symmetry plane) in excess of our values. This remains true even after a correction similar to that done for the gas is made. Since our gas densities agree with those of Kitamura after such a correction, and since we use *the same* method for gas and dust (differing in this from him), we suspect that there may be some inaccuracy in his dust results. We return to this below.

On the other hand, as evidenced on Fig. 3, our central dust density peak is much more pronounced here than in K90. This, combined with the preceding observation, suggests that the method used there for dust computations *smoothes out* the real dust distribution. This method is not completely described in K90, but, in answer to a question we addressed to him about it, Kitamura has indicated to us that he solved the dust equations in *nonconservative form*. In our opinion, this is the plausible cause of the mentioned smoothing: the vicinity of the interaction plane is singular for the dust distribution; thus, its treatment requires the use of the *conservative* formalism. In fact, there are steep dust density gradients away from the central region, too, so we believe that our conservative formalism shows the correct solution.

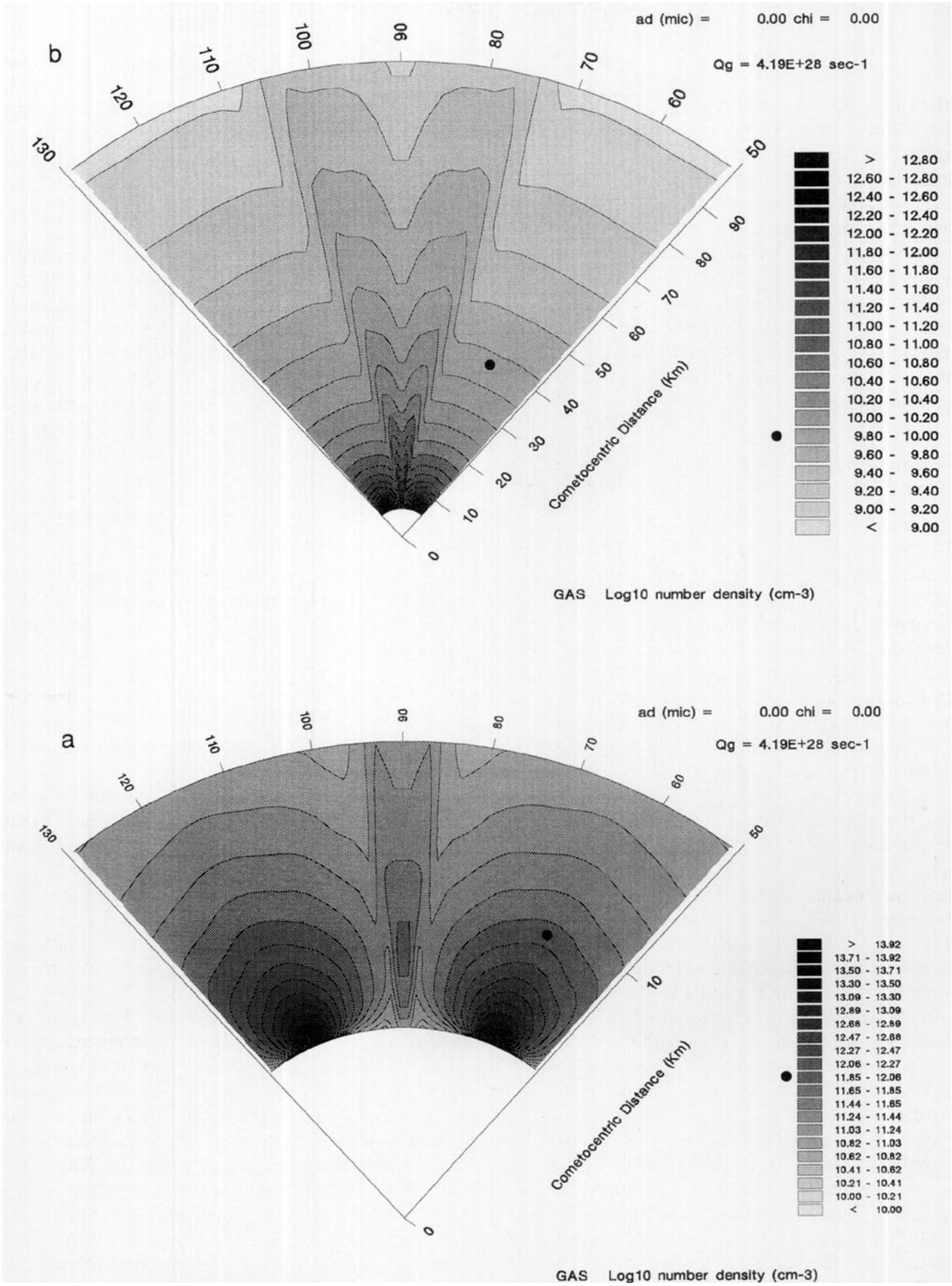

FIG. 2. Gas number density isocontours (cm^{-3}) at the plane $\phi = 90°$ in the case of two *pure* small gas jets. Parameters as in K90 (see Table I). For this and the following similar figures: (1) the top panel is the complete solution and the bottom panel is a magnification of the innermost part of it; (2) the large black dot matches one of the shaded area with its counterpart in the gray scale legend, for easier identification. In the top panel, the same isocontours as in K90 are used, for easier comparison.

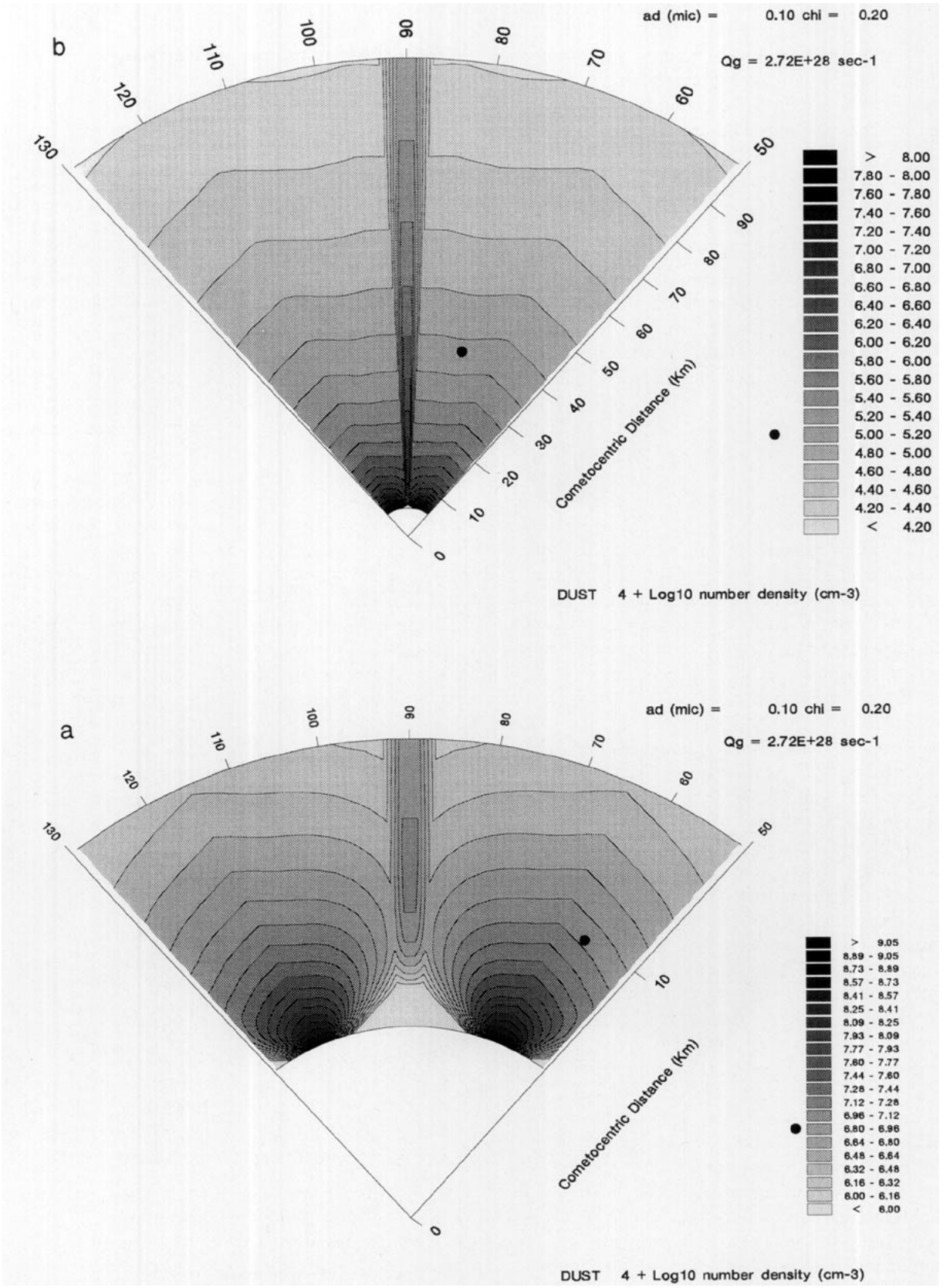

FIG. 3. Dust number density isocontours (cm^{-3}) at the plane $\phi = 90°$ in the case of two small dusty gas jets. Parameters as in K90 (see Table I). The computation is done using a two-fluid model as in K90. Notice that, for this and the other dust density displays, an integer number (here 12) has been added to the decimal logarithm of the density. In the top panel, the same isocontours are used as in K90. Notice the very sharp central "ray."

Now let us go back to this very narrow dust "ray": it seems legitimate to ask whether it is a physically credible result. This led us to question, for the first time (Rodionov 1994), the legacy of the two-fluid approach.

5.2.2. Difficulties with the two-fluid approach. In the preceding treatment (and all other single-size dust models), all dust particles are considered as a single fluid: there is no difference between the particles which have effused from differing active regions. Therefore, the calculation of the average dust parameters in the plane of the jet interaction (one of the symmetry planes) leads to the conclusion that the perpendicular component of the dust velocity is zero. Thus, dust particles can reach the jet interaction plane but cannot cross it or be reflected from it: this is equivalent to saying that the dust "adheres" onto the jet interaction plane. This is the source of the very sharp peak of Fig. 3.

It is clear that the accumulation of dust particles in this interaction plane is physically unacceptable: there is no process (even a gas shock) that could decelerate so fast *the dust*. Therefore this result, even though it was also obtained in K90, must be an artifact. The source of it can indeed be identified: the fluid approach (Euler equations here) is based on the concept of *fluid element averaging*; that is to say, given an elementary volume, and an additive parameter of the fluid (mass, momentum, energy), a net budget of this parameter is carried by summing the contributions of *all* particles of the fluid that cross the volume element. The normal physical meaning of this is that *mutual collisions between all the particles that cross the element* ensure the interchange of the additive quantities. Here, however, one is using the abnormal concept of "collisionless fluid"; this is permitted only after having carefully checked that all summations done (implicitly) at all points of the medium are physically acceptable. Such is the case, in practice only for particles that *share a common set of dynamical parameters* (Crifo 1991). Checking this amounts to solving at each point a so-called "Lambert problem," whereby one computes how many trajectories connect the point to the source of particles (Crifo 1994). Here, near the symmetry plane, clearly there exist two trajectories at each point: one from each active areas. Accordingly, *a three-fluid model must be used*: gas and two dust fluids (one per active region).

We believe that this problem must be often encountered in sophisticated dusty gas modeling efforts. In fact, for very complex geometries a large number of dust fluids (of the same size) may well have to be considered. As brought about independently to our attention by one of the referees of the present paper and by Kitamura in a recent discussion with us, using an "adequate number of fluids" is nothing but solving the collisionless Boltzman equation (in the external force field defined by the gas).

In the present case, the implementation of a three-fluid approach is a delicate procedure for the following reason: in the cells adjacent to the plane $\theta = 90°$ one naturally obtains those dust particles originating from the active region present in the computational domain and which exit the cell across this symmetry plane, but one does, of course, not obtain the mirror symmetric ones that (in reality) would penetrate into the cell, arriving from the (here virtual) symmetric active region. Thus, in those boundary cells, one prescribes free outflow of the particles from the first fluid, together with an automatic inflow of symmetric particles (virtually coming from the other area).

Isolines of the dust density calculated in three-fluid approach are shown in Fig. 4. One sees that the central "ray" has disappeared, replaced by a broad, paradoxical "jet" bounded by bright limbs. The physical source of this "paradoxical" structure will be discussed later.

Figures 5 and 6 compare the gas distributions obtained under the two-fluid and the three-fluid approaches. The main difference between these two solutions is that the narrow central gas density depletion obtained in two-fluid approximation (and in the pure gas solution) has almost disappeared from the three-fluid solution. Here again, the exact explanation is complicated: let us say only that the disappearance of this structure (compared to the pure gas case) follows from the presence of a smooth distribution of fine dust across the "secondary gas jet." In the two-fluid case, such a smooth distribution is absent, most of the dust being trapped in the symmetry plane.

Except for the disappearance of this central structure, one can also notice that the presence of dust has slightly broadened the secondary gas jet. However, crudely speaking, the pure gas and dusty gas distributions are rather similar.

5.2.3. Conclusion of the comparison with K90. For computing the gas component of a coma, both the Osher scheme of K90 and the present method give equivalent results under the condition that the grid meshes be adjusted to give equivalent accuracy.

For computing the dust distribution, a single-fluid approach is suitable in trivial geometries, but in general a specific multifluid method adjusted to the geometry of the problem (Boltzman equation) must be used, and the dust equations must be integrated in conservative formalism.

5.2.4. Effect of the dust particle size. Isocontours of the gas and dust density are presented in Figs. 7 and 8, for the same problem, except that the dust grain radius is now $a_s = 1$ μm. By comparing the results with those given of Figs. 6, one sees that the increase in dust particle size hardly affects the gas density, except in the central narrow region of density decrease (notice that the difference in isocontour position is due to the difference in total

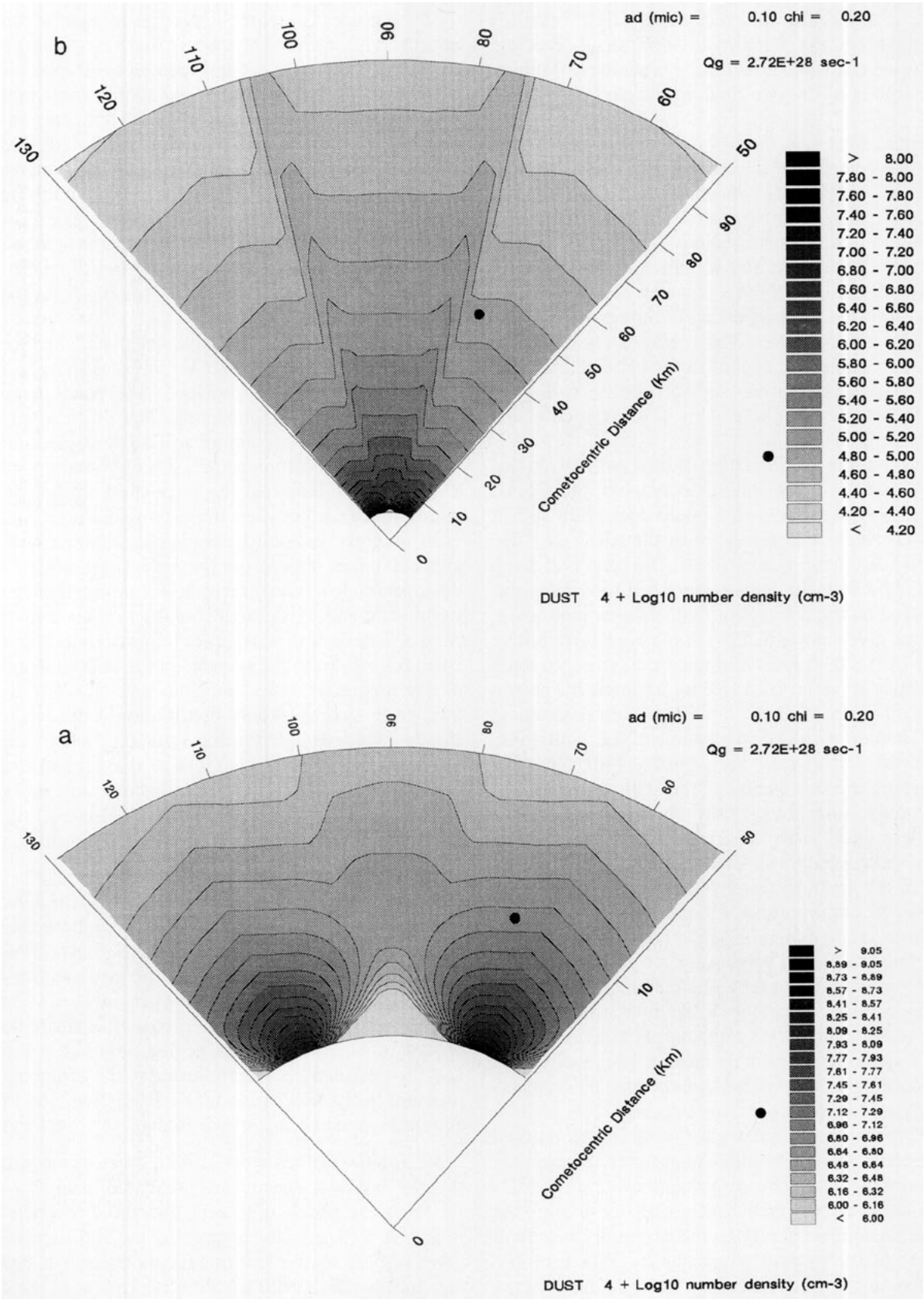

FIG. 4. Same as Fig. 3, but now the computation is done using a three-fluid model. The central, sharp "ray" has disappeared. In the top panel, the same isocontours are used as in K90.

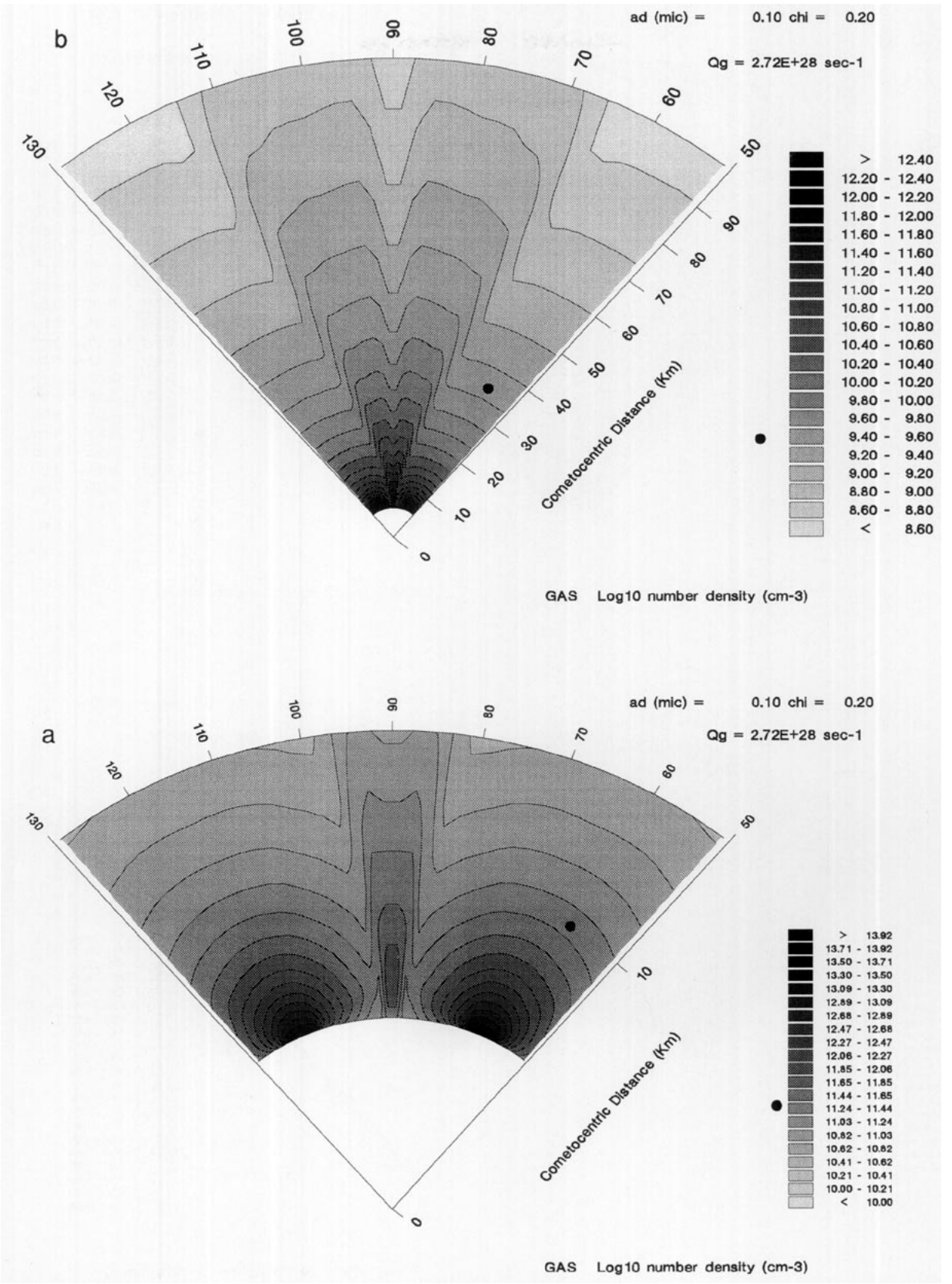

FIG. 5. Gas number density (cm^{-3}) at the plane $\phi = 90°$ in the case of two small dusty gas jets; parameters as in K90. The computation is done using a two-fluid model. In the top panel, the same isocontours are used as in K90.

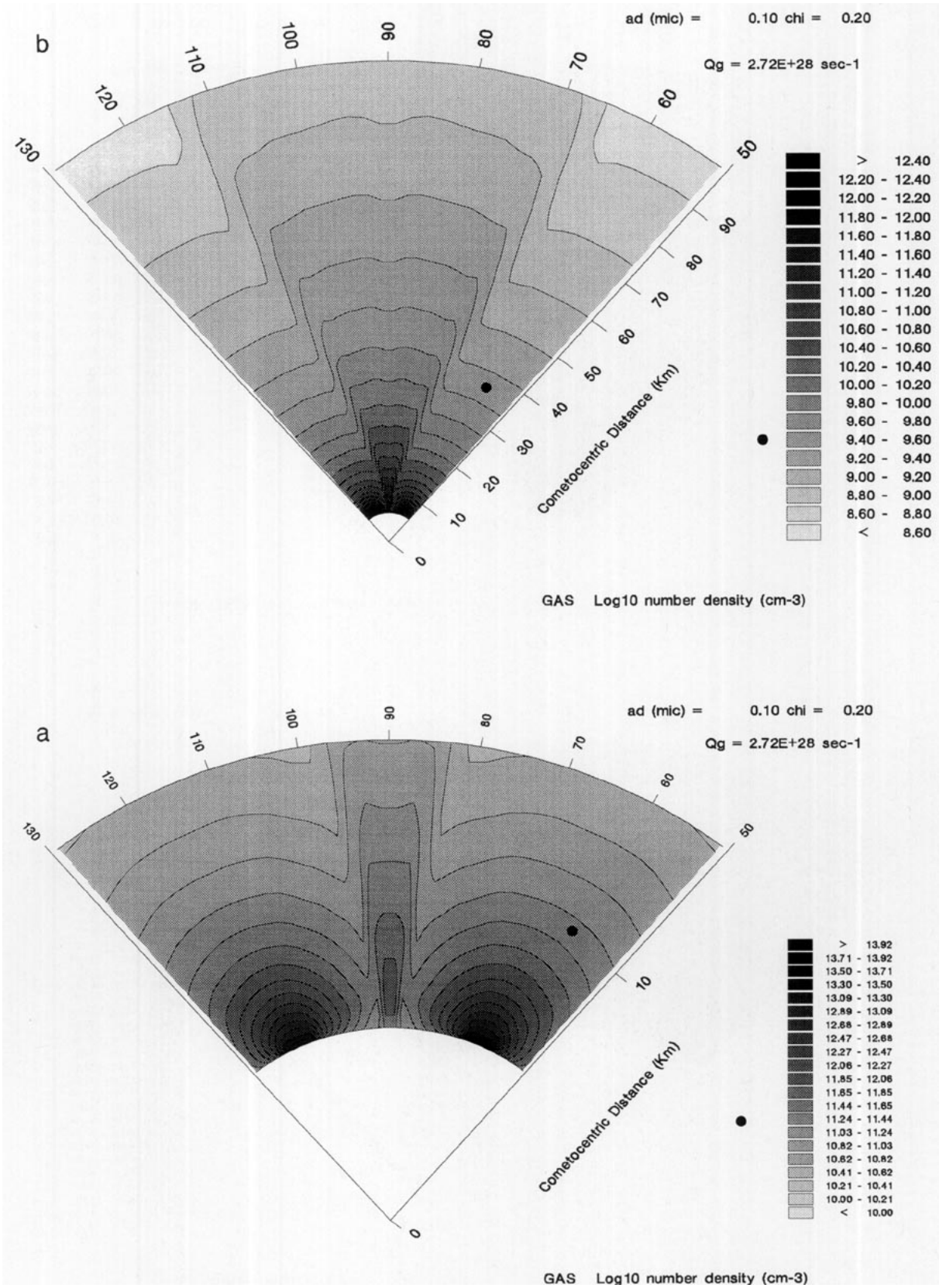

FIG. 6. Same as Fig. 5, but now the computation is done using a three-fluid model. In the top panel, the same isocontours are used as in K90.

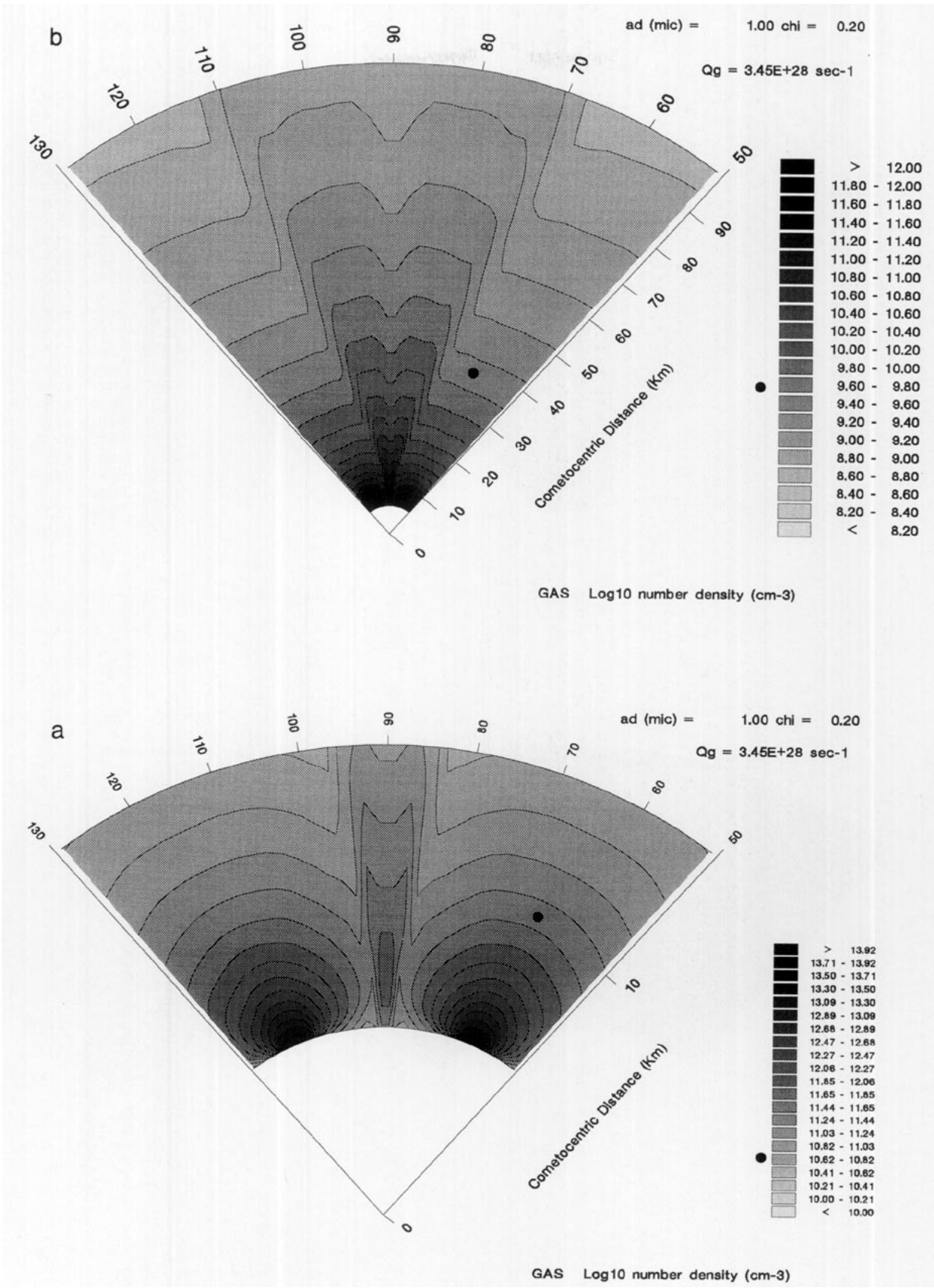

FIG. 7. Gas number density isocontours (cm^{-3}) at the plane $\phi = 90°$ in the case of two small dusty gas jets. Parameters as in K90, except that $a_s = 1$ μm. In the top panel, the same isocontours are used as in K90.

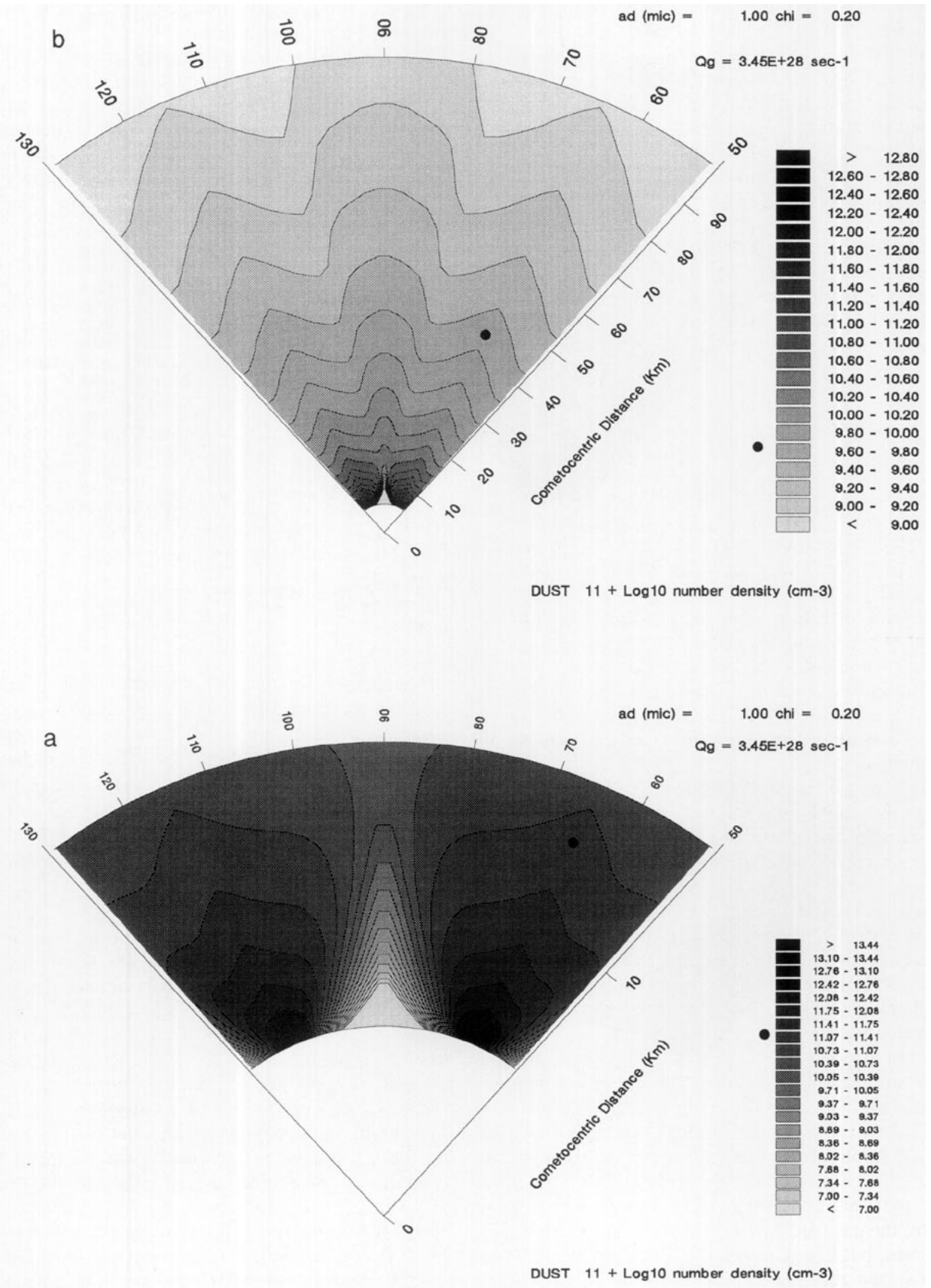

FIG. 8. Dust number density isocontours (cm^{-3}) for the same problem as in Fig. 7. In the top panel, the same isocontours are used as in K90.

production rate—see Table I). The comparison with Fig. 4 shows that, on the other hand, larger dust particles are less easily deflected by the gas, so their density distribution follows a little better their surface production pattern. Yet the global dust distribution still contains a conspicuous, broad paradoxical central jet.

5.2.5. Effect of the distance between the active regions. Figures 9 and 10 present the gas and dust densities calculated for the same problem, with $a_s = 0.1$ μm again, but with an angular distance between the jet centers decreased down to 30°. One sees that this decrease broadens in the θ direction the central secondary gas jet. In contradistinction with it, the central, paradoxical dust jet becomes narrower; also, the edges of this jet become very bright.

5.3. Interaction between Three Identical Dusty Jets (Conditions Close to Those of K90)

Figures 11 and 12 present the gas and dust density isocontours in a coma formed by three identical jets in a symmetrical configuration with respect to the plane $\theta = 90°$. The geometrical parameters are given in Table I ("three small jet case").

A four-fluid formalism is used. In accordance with the treatment at the symmetry plane described precedingly, this amounts to considering gas and only two dust fluids: there is no place where dust grains originating from all three active areas are simultaneously present.

The gas density distribution (Fig. 11 and color plate) is very complicated.

Concentrating, first, on the lowermost region (Fig. 12, bottom panel), and comparing with Fig. 9, one observes the formation of two nearly independent two-jet interaction structures (diedres of standing plane shocks emanating from $\theta \simeq 75°$ and from $\theta \simeq 105°$). The two volumes of shocked gas expand outward, forming secondary supersonic "daughter" jets. On Fig. 11 (top panel), one sees that these secondary jets meet with one another at the symmetry plane near $r = 20$ km, forming a secondary V-shaped shock structure centered on the symmetry plane. This secondary structure encloses what can be called a third-generation gas jet. Thus, the coma is structured by nested jet interactions: primary surface jets forming secondary jets which form third-generation jets. In a very strong comet with many active areas, it is possible that fourth-generation jets (or higher?) appear at higher altitudes.

If one adds that an imprint of the dust pattern is also carried by the gas (the dips near $\theta = 65°$ and 115° in the present case, but in a real comet all sizes will bring their signatures) one recognizes that the resulting gas coma structure—a broad fan of emission with many fine structures—becomes rather difficult to decipher in terms of nucleus production patterns.

The dust density isocontours are shown on Fig. 12 (and also on the color plate). The dust patterns closely resembles two side-by-side close-interaction fine dust structures (as in Fig. 10). An interpretation of the global dust patterns using a simple-minded approach will be "two strong dust jets bounded by narrow bright dust rays, superimposed on a hemispherical background": hardly any relation to the real structure.

5.4. Physical Relevance of the Preceding Solutions

The values of Q used ($\simeq 3$–4×10^{28} sec^{-1}) should be compared to the total production Q in P/Halley at the time of the flyby mission $\simeq 7 \times 10^{29}$ sec^{-1}.

In this respect, the justification for ρ_0 made by page 459 of K90 is misleading: it suggests that $Q = 10^{30}$ sec^{-1}. However, it would be so only *if the nucleus was uniformly emitting and of radius 2 km* or if the present nucleus, of radius 6 km, was emitting *over 1/9 of its surface*. In reality, in K90 this nucleus emits over $\simeq 2$ km^2, i.e., over $\simeq 1/(72\pi)$ of its surface only, whereby Q is much smaller than suggested.

It is possible to interpret the preceding results in several ways:

- A representation of a P/Halley-like comet if it really is a mosaïc of $\simeq 20$ *evenly distributed and closely similar* active areas of the present kind; this is unlikely.
- A representation of part of P/Halley surface, but which produces only a minor fraction of Q, the bulk of it being produced differently *and far apart* from it.
- A possible typical configuration for a moderately active comet, such as those considered as suitable targets for the future Rosetta mission.

Since the preceding solutions are more suitable for characterizing a modest comet, we have also found of interest to present three additional solutions which correspond to water production rates comparable to the P/Halley flyby value. For the same reason, we have also changed the dust representation: new values of χ and a_s (see Table I) that approximate more satisfactorily the gas–dust interaction corresponding to the *in situ* measured P/Halley dust size spectrum are chosen (see Appendix A). It turns out that the new dust size is also of greater interest to the interpretation of visible and IR observations than the small value 0.1 μm was.

We have varied the geometry of gas and dust production, distributing the latter between one, two, and three jets (the single jet case is of interest to the global understanding of the formation of the coma structures).

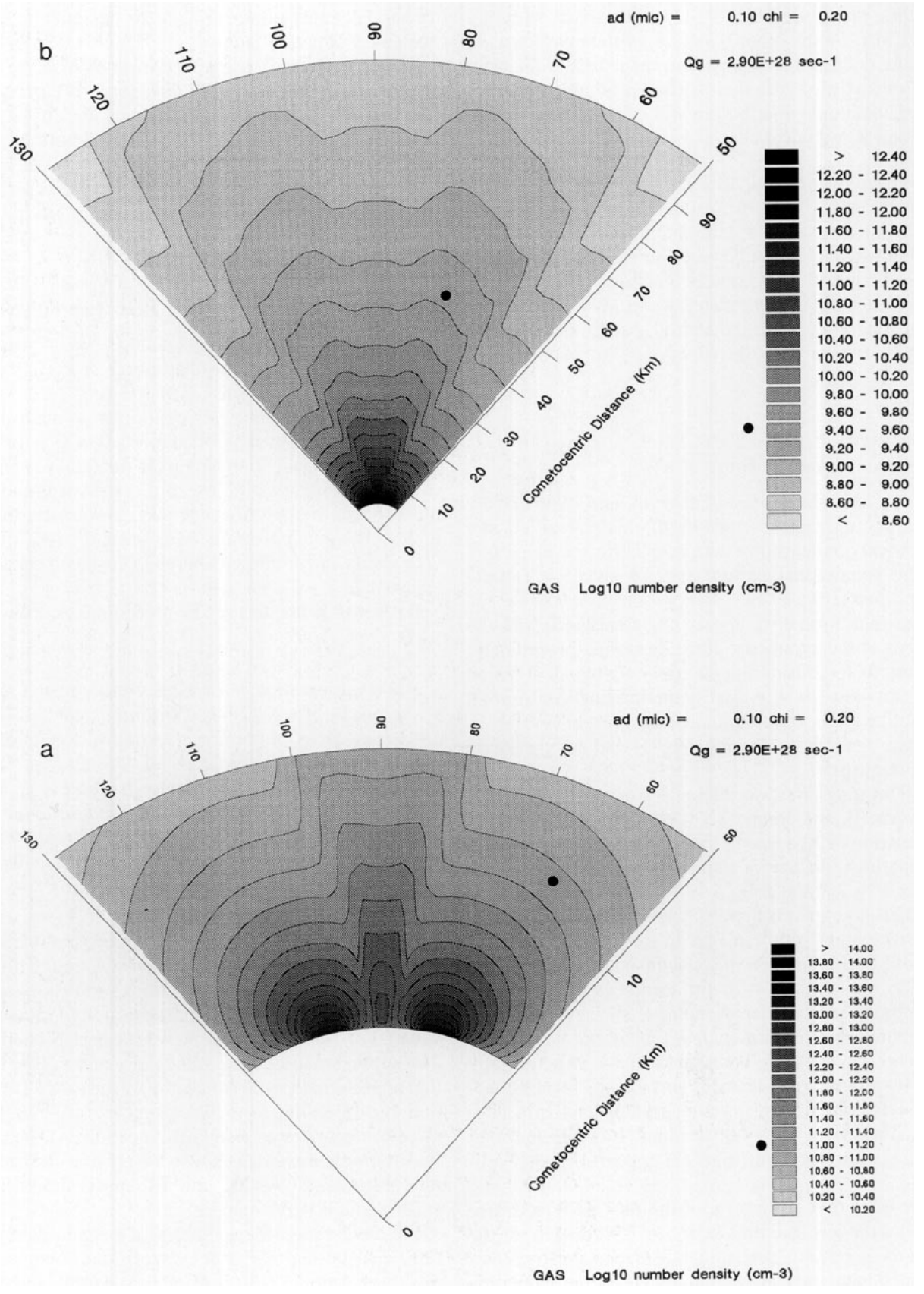

FIG. 9. Gas number density isocontours (cm^{-3}) at the plane $\phi = 90°$ in the case of two small dusty gas jets. Parameters as in K90, except that the angular distance between the centers of the jets is here 30°. In the top panel, the same isocontours are used as in K90.

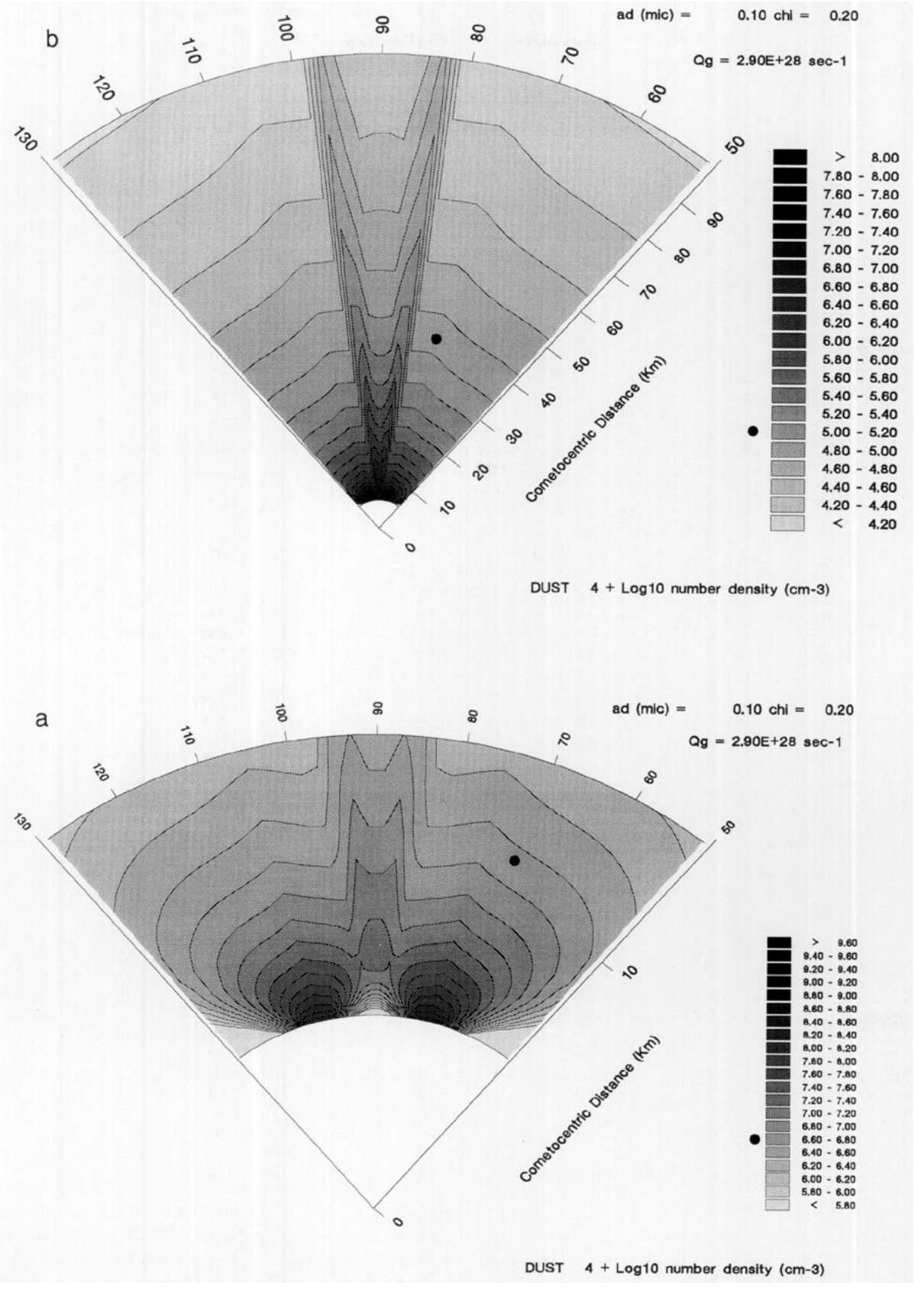

FIG. 10. Dust number density isocontours (cm^{-3}) at the plane $\phi = 90°$ for the same problem as in Fig. 9. In the top panel, the same isocontours are used as in K90.

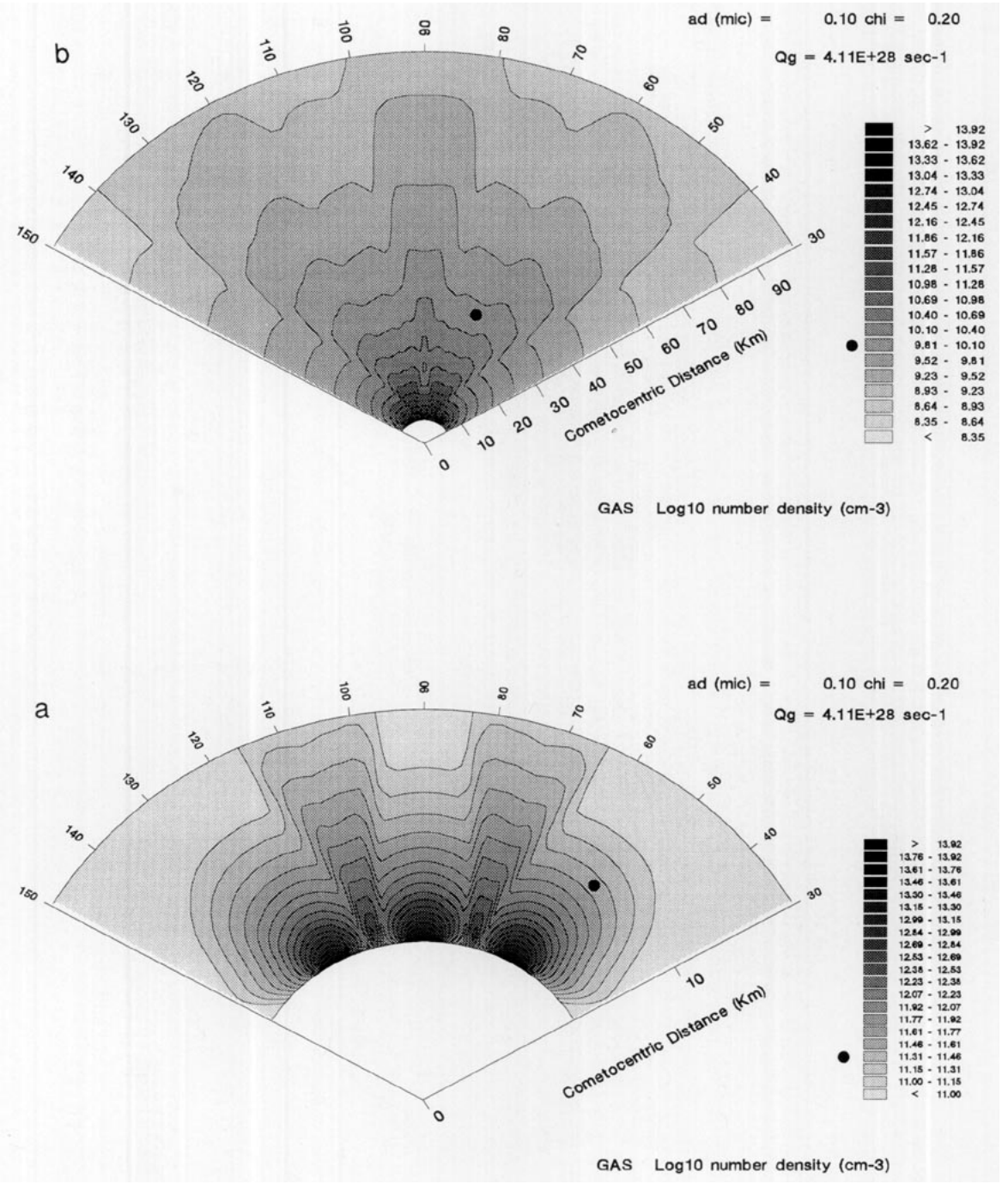

FIG. 11. Gas number density isocontours (cm^{-3}) at the plane $\phi = 90°$ in the case of three small dusty gas jets. Parameters as in K90, except that there are three active areas.

5.5. *Dusty Gas Jet Interactions in a P/Halley-Like Comet*

The following results correspond to a high total gas production (Table I). We start by showing a single-jet coma, which, aside from its intrinsic interest, can serve as a reference for comparison with the multijet solutions.

5.5.1. Single jet solution. Figures 13 and 14 show the structure of the coma produced by a single spherical square. In addition to density isocontours, gas and dust velocity fields are also shown by a distribution of arrows.

The gas distribution is smooth, with no apparent structure: it obeys the general quasi-spherical behavior men-

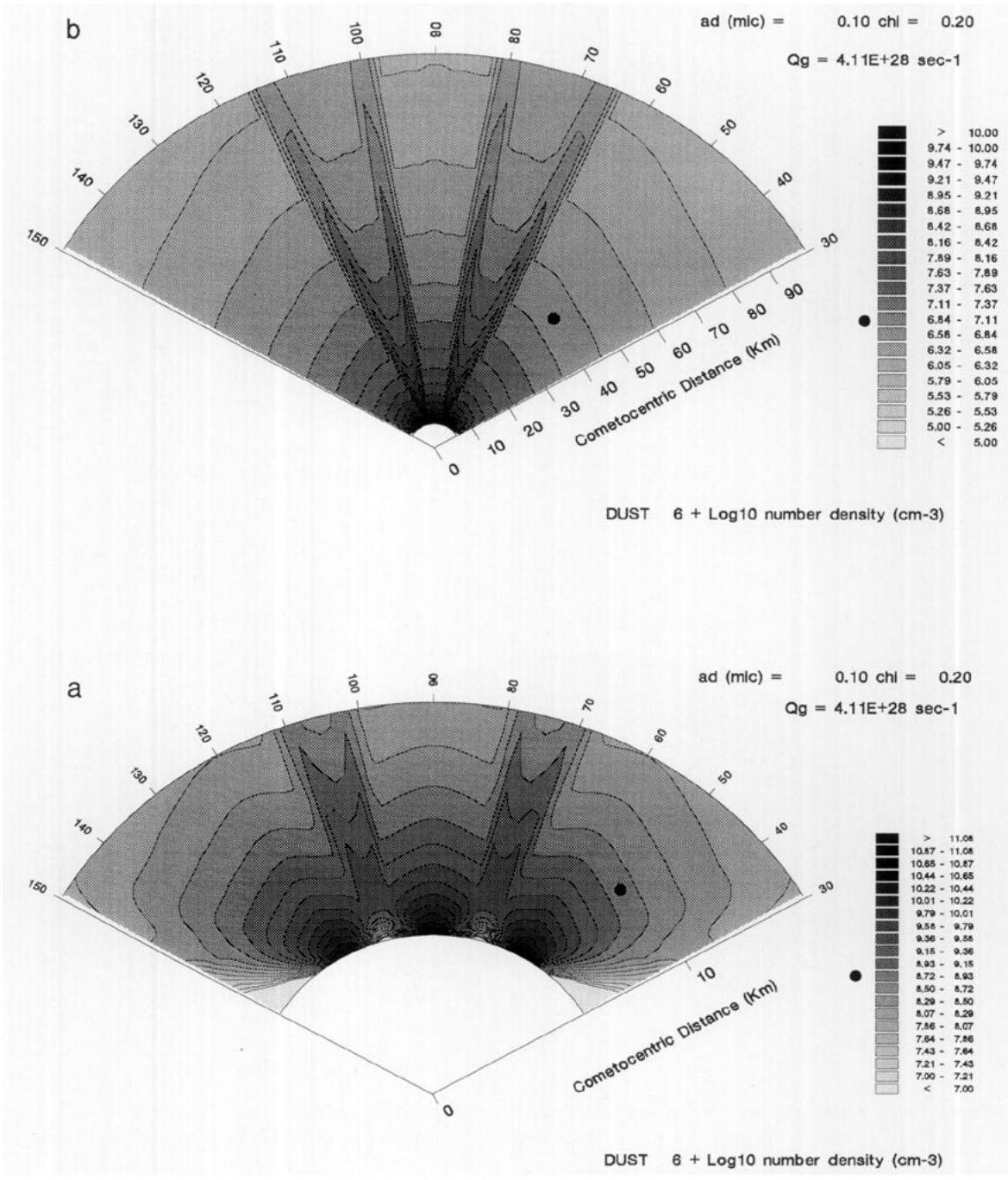

FIG. 12. Dust number density isocontours (cm^{-3}) at the plane $\phi = 90°$ for the same problem as in Fig. 11.

tioned in Section 5.1. Thus, from the observational point of view, a single-jet *gas* coma cannot be easily distinguished from an isotropic coma. In contrast with this, the sunward dust distribution is markedly fan-like; the dust is not carried far into the rear side of the coma.

The present solution bears some similarity with two solutions published precedingly: in Kitamura (1987), Fig. 6, and in Körösmezey and Gombosi (1990), Figs. 5a–5e. We will refer to these two solutions as "K87" and "KG90."

In K87, a dusty jet characterized by $Q \simeq 3 \times 10^{28}$ sec^{-1}, $\chi = 0.3$, and a mixture of dust grains with three differing radii (0.01, 0.1, and 1.0 μm) issues in vacuum from a circular active area of radius 1 km situated on a spherical

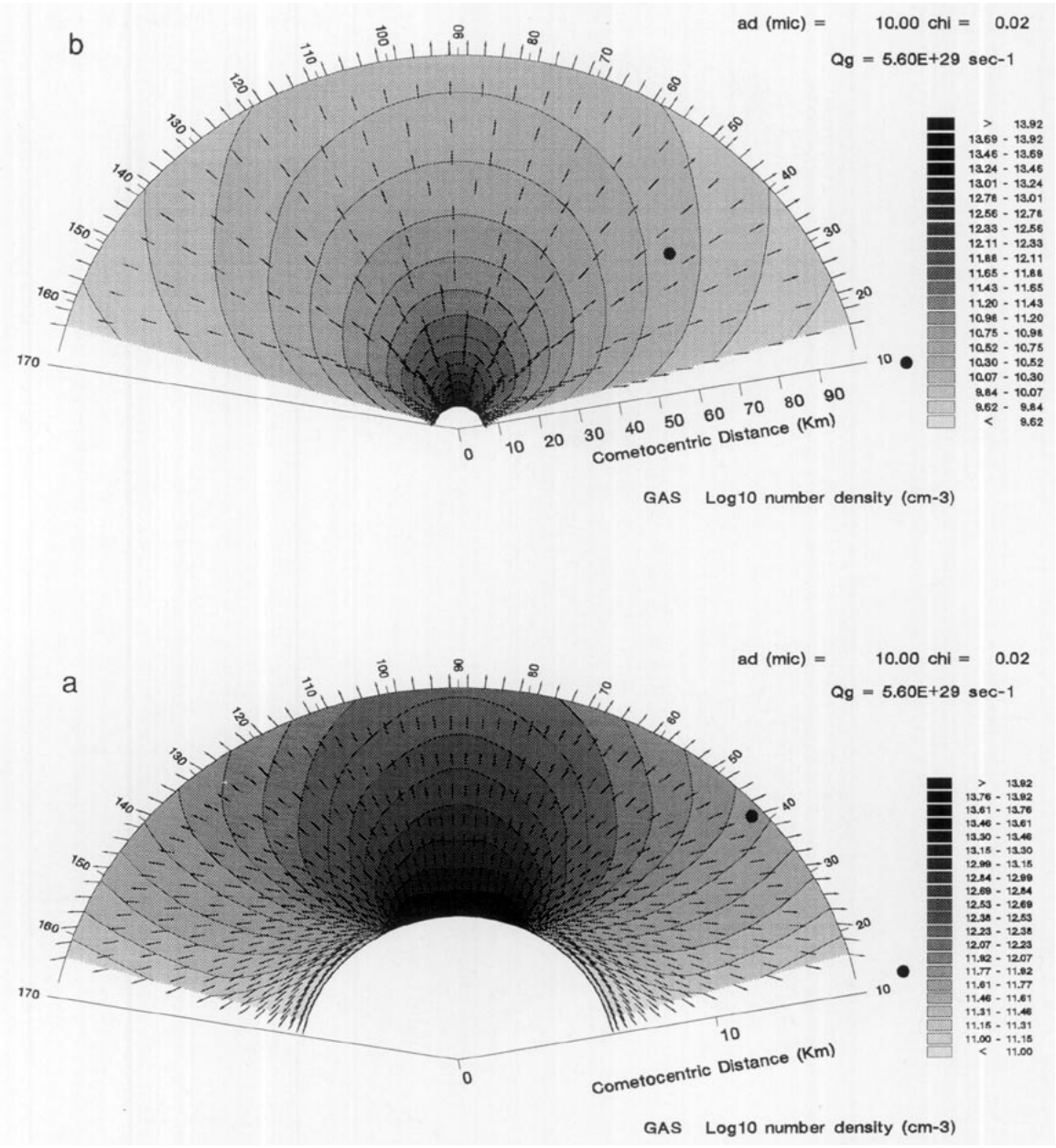

FIG. 13. Gas number density isocontours (cm^{-3}) in the plane $\phi = 90°$ in the case of a single large dusty gas jet. The parameters approximate P/Halley flyby conditions. Gas velocity vectors are also shown. The largest velocity visible in the bottom panel corresponds to about 1 km sec^{-1}.

nucleus with radius 6 km. (Notice that in KG90 this solution is mistakenly referred to as a strong Halley-like solution. We have explained above the origin of this misconception.) The gas isodensity contours of K87 resemble those in our present computation; such is not the case, apparently, of the 1-μm dust isocontours, which extend deep into the nightside region, whereas our 10-μm contours do not. We suspect that the difference in dust grain mass alone is not sufficient to explain such a discrepancy: the difference in χ, which results in a great difference in the extent of the initial subsonic gas flow region, must also come into play.

In KG90 a second-order Godunov-type method in many respects similar to the present one is used to derive true time-dependent solutions. We can therefore compare our solution only with the solution shown there at the largest time. In one case, a cylindrically symmetric dusty jet characterized by $Q = 5.3 \times 10^{29}$ sec^{-1}, $\chi = 0.3$, and $a_s = 0.65$ μm, and by a Gaussian surface emission profile (FWHM of 16.6°) emanates from a 6-km-radius spherical

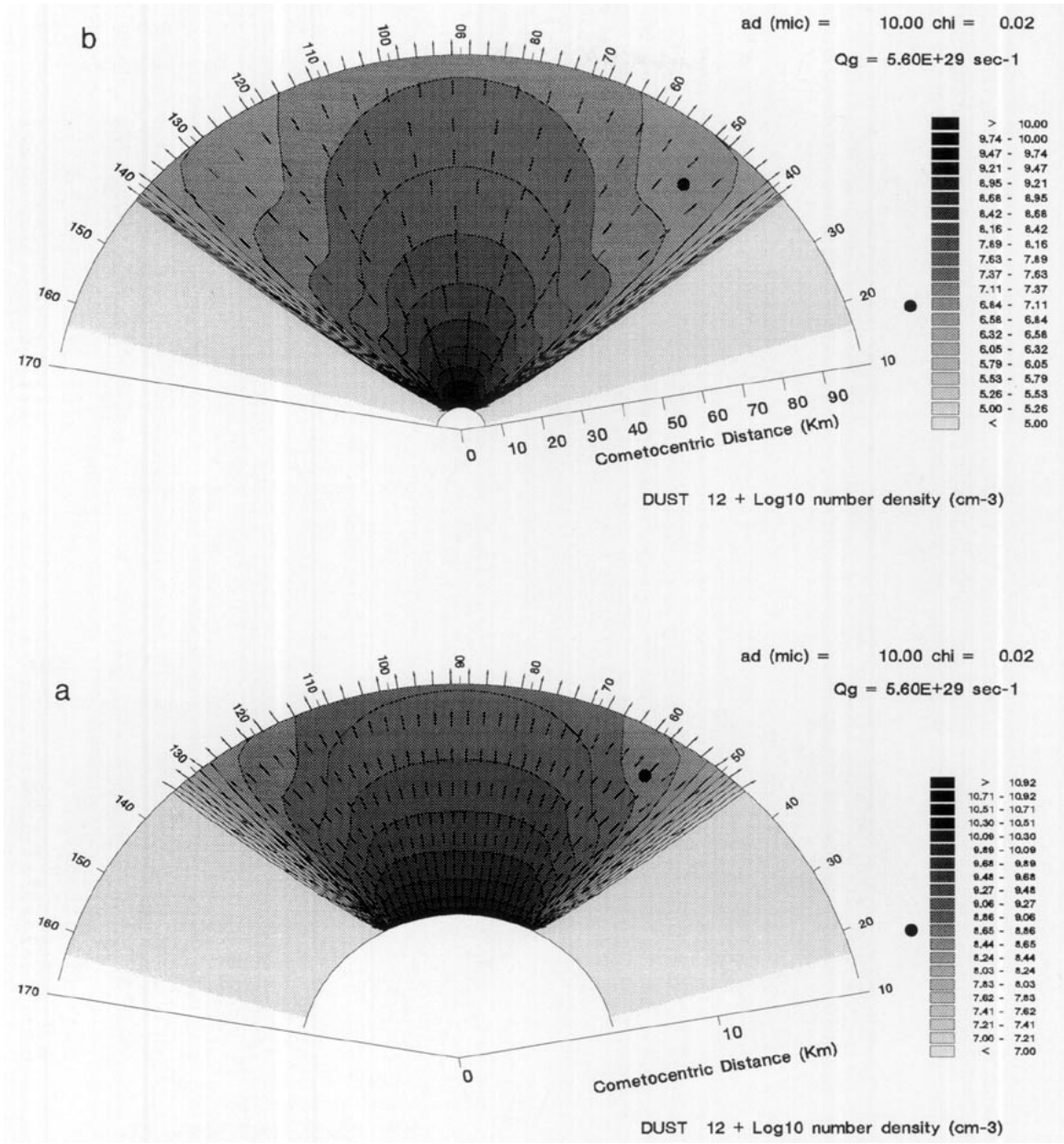

FIG. 14. Dust number density isocontours (cm^{-3}) and flow velocity vectors for the same problem as in Fig. 13.

nucleus also producing a diffuse background of dust and gas. Due to the presence of the background, our solution cannot be compared with KG90 on the antisolar side. However, near the jet axis the existence of this background is likely immaterial. The solution in KG90 (Fig. 5e, $t = 400$ sec) shows a strong narrow "nose-like" axial dust density peak, associated with a pronounced "conical depression" in gas density (Fig. 5b). This is quite in contradiction with our *steady* results. However, KG90 have also shown results for a smaller jet (Figs. 4a–4e) and for longer times. At $t = 800$ sec, the "small jet" gas hollow cone and dust spike have nearly vanished: we suspect that this must also be true for the "large jet" solution, when sufficiently long times are considered.

5.5.2. Two-jet solution. Figures 15–17 present the density on the plane $\phi = 90°$ in a coma in which a production rate nearly equal to the previous one is due to two equal active areas. The angular distance is slightly larger than in K90, but the size of the areas is much greater (see Table I). Notice that χ is also smaller than in K90.

Comparing with Fig. 7 (1-μm-size dust) one sees that

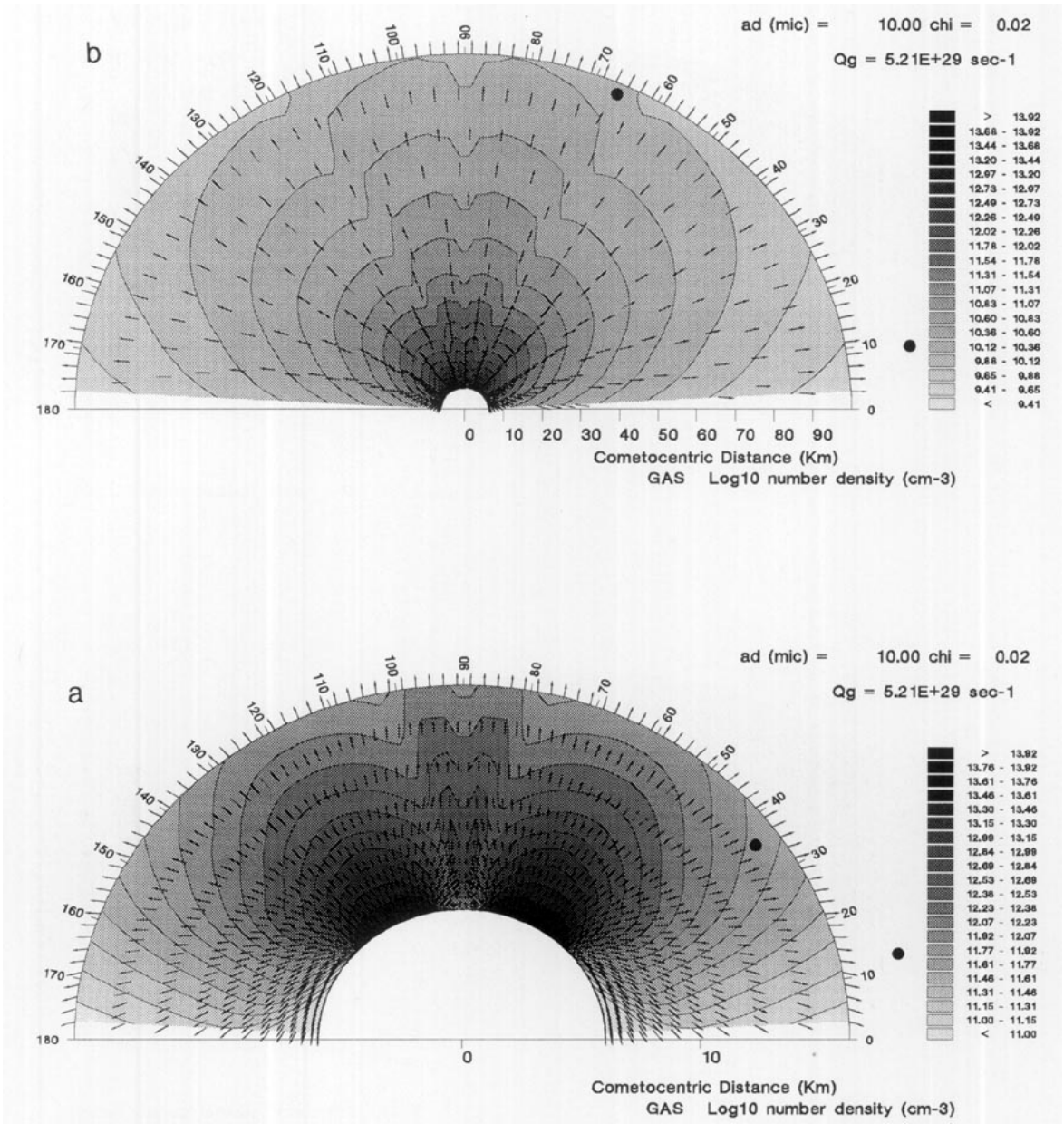

FIG. 15. Gas number density isocontours (cm^{-3}) and velocity vectors, in the case of two large jets. The parameters approximate P/Halley flyby conditions. Notice the gas stagnation region at about $r = 8$ km and $\theta = 90°$.

the 20-fold increase in gas production rate has practically not affected the global gas density pattern (the "secondary" gas jet has only been slightly broadened and the central density depletion slightly reduced).

Examination of the gas velocity field (Fig. 15, bottom) reveals the existence of a gas stagnation region over the surface, between the active regions. Notice also that the gas flow direction is not in general transverse to the isodensity contours as is sometimes naïvely assumed.

The 10-μm-radius dust density distribution is shown on Fig. 16. Comparing with Fig. 8 (1-μm dust), one sees that the innermost structures are similar, but not the outermost ones: here, one has the impression of two broad dust jets on the normal of the active area, enclosing a central pair of rays, while precedingly it was rather a strong central jet bounded by two weaker jets. However, the geometry is the same.

Figure 17 allows an understanding of the formation of the dust density patterns. The uppermost and middle panels show, on two differing scales, the isodensity contours *of the right dust fluid alone*. Comparing with the density contours of Fig. 14 (single jet from a larger geometrical

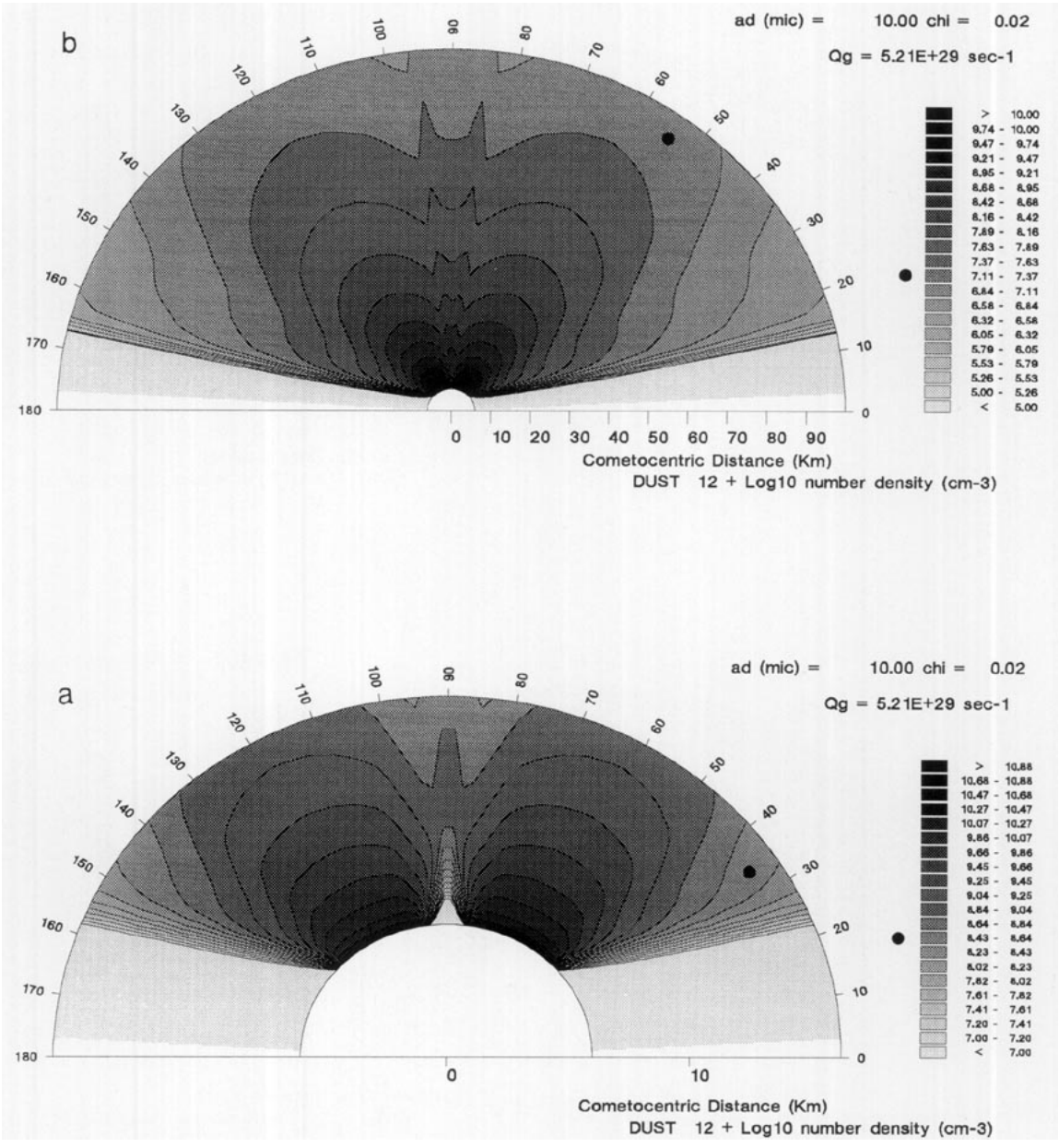

FIG. 16. Dust number density isocontours (cm^{-3}) for the same problem as in Fig. 15. Velocities are not shown, because in the interaction region two distinct velocity vectors exist at each point.

area), it is seen that the *left side* of the distribution is now "compressed," forming a ray. The superposition of the left and right isodensities then produces the central "abnormal jet" with its bright edges. The expression "compressed" used above is inadequate: it is essential to always keep in mind that the dust–gas interaction is limited to the first kilometers above the surface. Thus, what happens here is that, *in the first 2 km above surface*, the left side of the right dust fluid is *deflected* toward a more vertical direction by the gas from the left area (and vice-versa); this appears clearly from the dust velocity plot (Fig. 17, bottom).

Beyond this initial region, the evolution of the dust patterns continues "by itself," i.e., practically like in a vacuum; it can be compared to the change in density pattern of a group of marathon racers, as time goes on. It does not make physical sense to call jets such *dust* patterns which do *not* trace dust motions. In the first kilometers, there are *distinct* directions of flow for the two dust fluids at the same point in their common region;

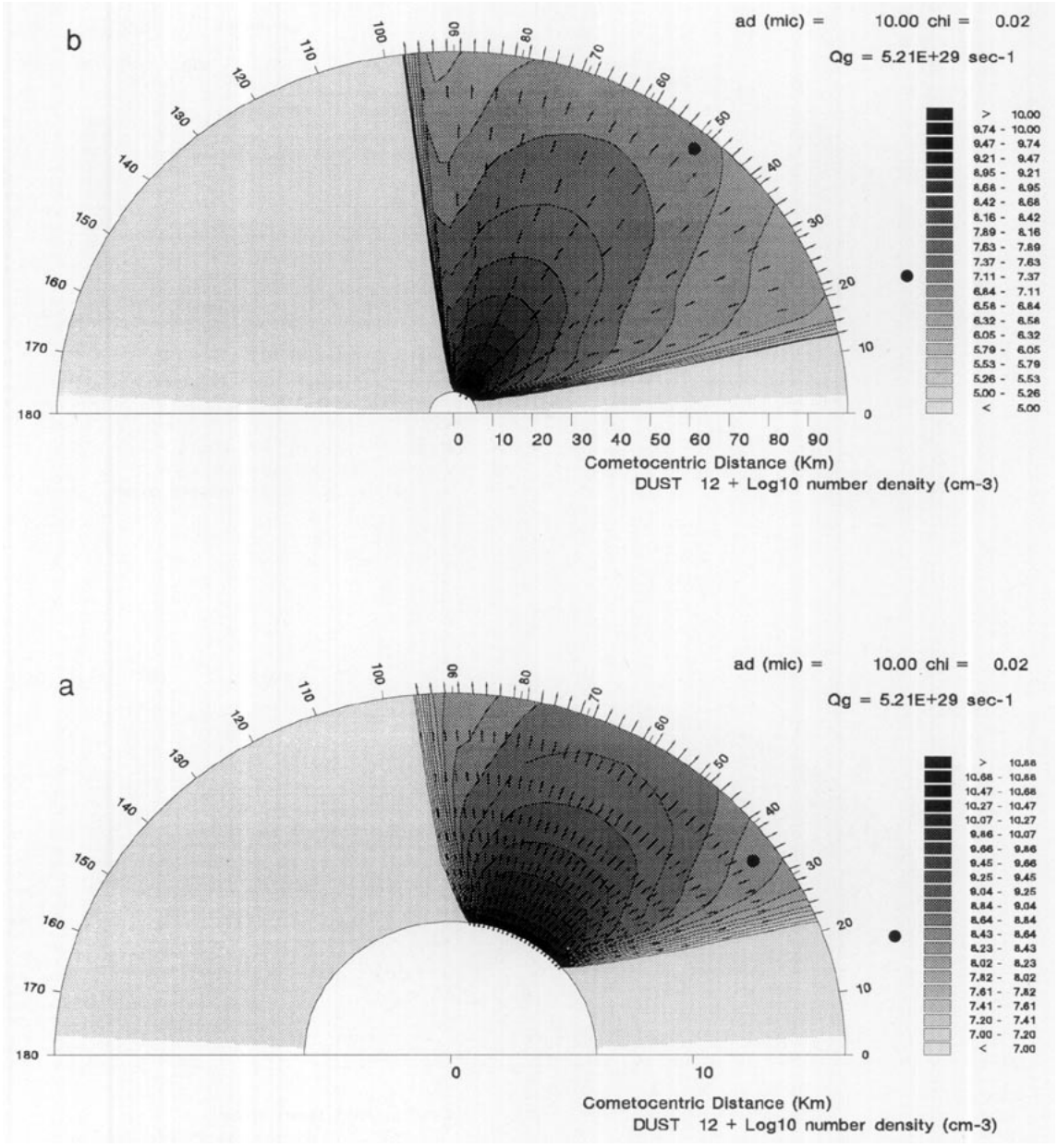

FIG. 17. Dust number density isocontours (cm^{-3}) and velocity vectors, in the plane $\phi = 90°$, and for the same conditions as in Figs. 15 and 16. Here, only the dust emanating from the right side area is shown. By comparison with Fig. 14, one can see the distortion due to the presence of the left side area. The superposition of the present isocontours with mirror-symmetric ones due to the left area explains the patterns of Fig. 16.

at higher altitudes, the dust flows practically radially, convecting with it density isocontours that are inclined at varying angles with respect to the dust direction of motion.

5.5.3. Three-jet solution. Figures 18 to 21, and the color plate, present gas and dust density isocontours in the plane $\phi = 90°$ for *three* identical active regions symmetrically located with respect to the plane $\theta = 90°$. The geometrical parameters are given in Table I. Compared with the solution of Figs. 11–12, the active areas and their angular separation are larger (see Table III).

The gas patterns, at first sight, seem very different. However, closer examination reveals that this is mostly a *scaling* problem: the nested interactions described precedingly are easily recognized, but on a geometrical scale increased by a factor $\simeq 3$. For instance, the "dark spot" at which the "secondary" gas jets meet to form the "third generation" gas jet apex is at about $\theta = 90°$, $r = 20$ km in Fig. 11 and at about $\theta = 90°$, $r = 60$ km on Fig. 18.

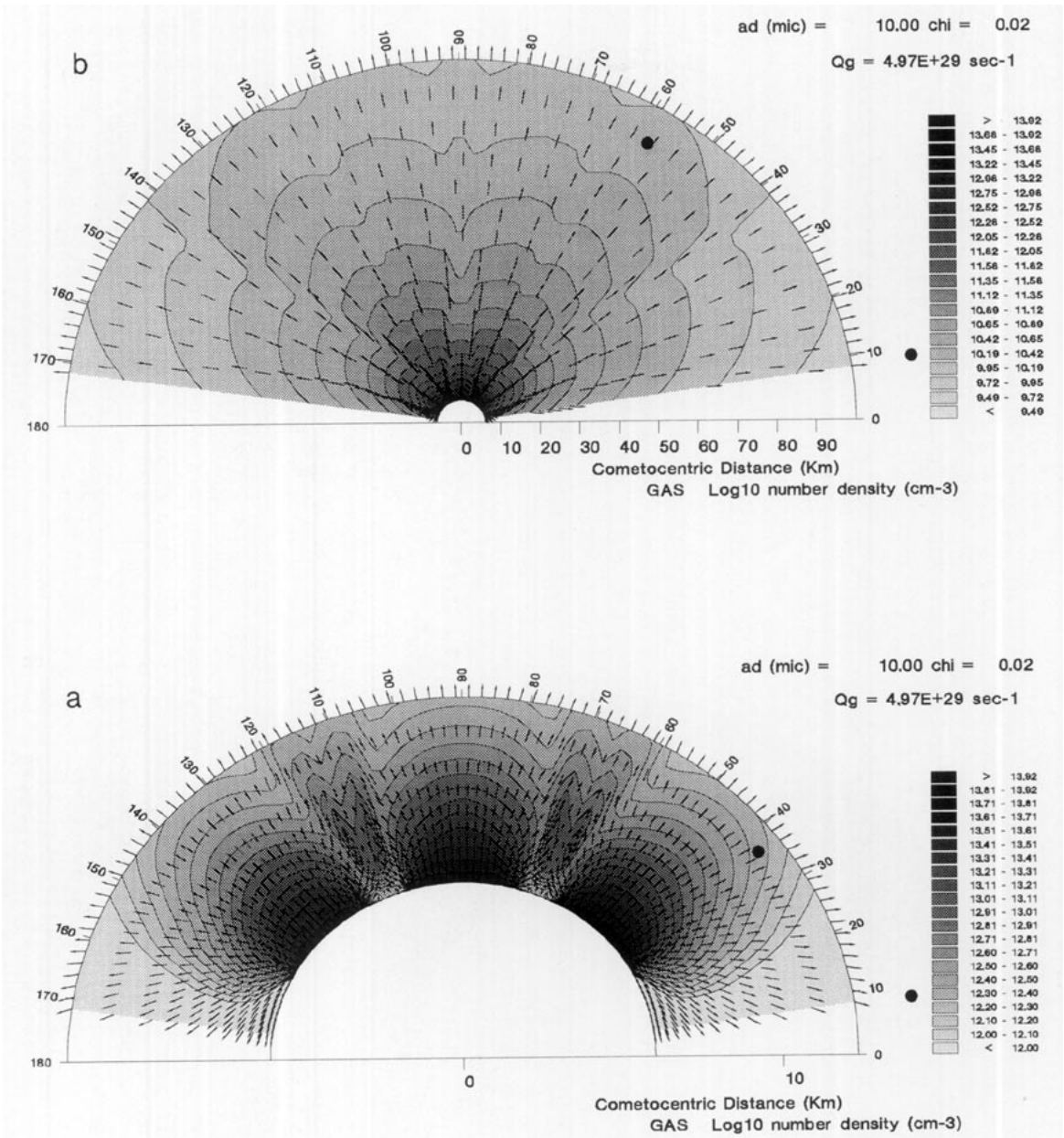

FIG. 18. Gas number density isocontours (cm^{-3}) and flow velocities, in the plane $\phi = 90°$, and in the case of three large dusty gas jets. The parameters approximate P/Halley flyby conditions.

This of course suggests making a dimensional analysis of the model equations in the future.

The same preceding remark is true for the dust patterns. For instance, the formation of bright limbs on the sides of the two paradoxical dust jets starts at $r \simeq 10$ km in Fig. 12 and at $r \simeq 25$ km in Fig. 19.

However, the large difference in dust mass has also marked implications: the paradoxical jets are less pronounced in Fig. 19 than in Fig. 12, and there are bulges at the vertical of the active areas on Fig. 19, not in Fig. 12.

Figures 20 and 21 show, respectively, the central dust fluid density and the left and right dust fluid density. They allow exactly the same interpretation of the resulting dust patterns that was provided for two jets in Fig. 17.

6. DISCUSSION

Figure 22 summarizes the most elaborate results obtained here, *viz.* the three-jet interactions. We believe that it illustrates very well what the problem of identifying nucleus features from coma gas or dust patterns consists

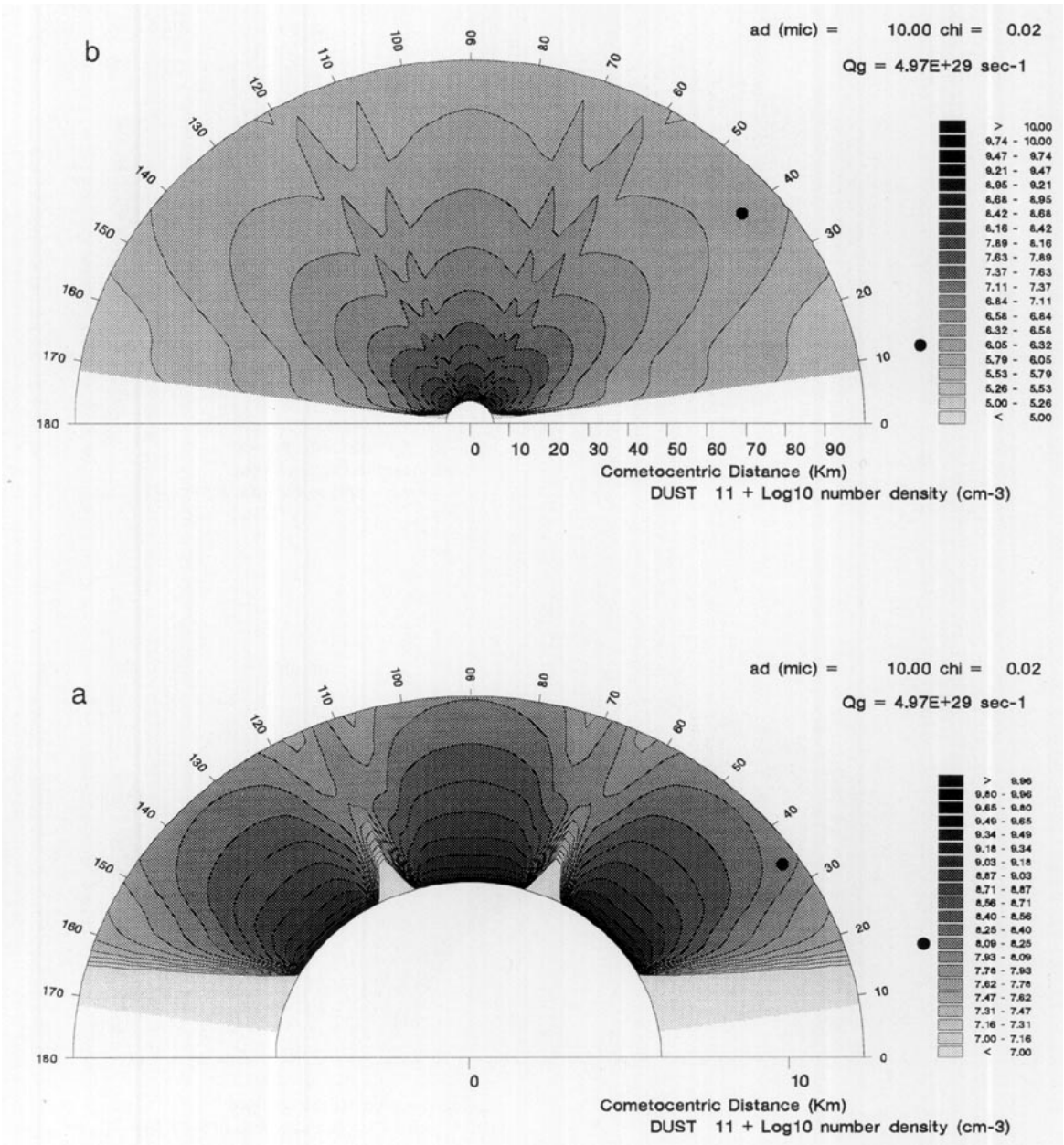

FIG. 19. Dust number density isocontours (cm^{-3}) at the plane $\phi = 90°$ for the same problem as in Fig. 18.

of. In using these figures, it must, in addition, be kept in mind that these are not *images*, but gas or single-size dust density patterns in a plane. In images, the superposition of a broad distribution of sizes is observed, each one with its genuine structure, and line-of-sight integration is made.

6.1. *On the Interpretation of Coma Gas Patterns*

Let us first recognize that the gas patterns computed here are H_2O patterns, not currently accessible to direct observations. The general impression one can get from these patterns is that, excepting the first hundred meters away from the active surface, they do not reveal in a straightforward way the nucleus production map. It is plausible that, as shown by Kömle and Ip (1987) in a simple case, gas density structures are preserved far out in the coma, but the interplay of signatures from the complex topology of a real nucleus likely will produce a very cryptic pattern.

A different question is whether the jet-like patterns observed in the emission lines of minor constituents of

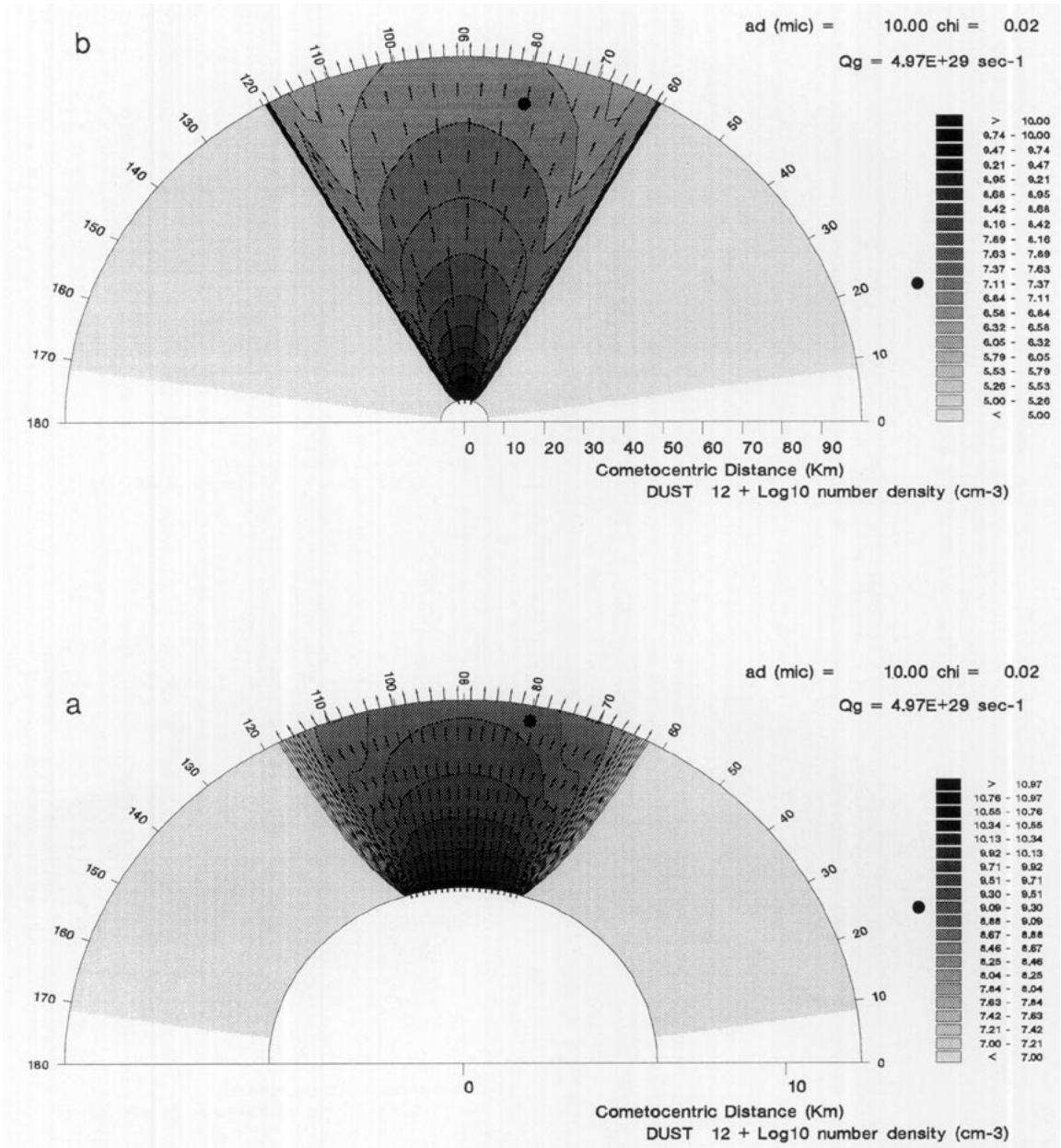

FIG. 20. Dust number density isocontours (cm^{-3}) and flow velocity for the same problem as in Figs. 18 and 19. Only the dust emanating from the central active area is shown. By comparison with Figs. 14 and 17, one can see the distortions due to the presence of the left side and right side active regions. Superposition of the present isocontours and of those of Fig. 21 explains the structure of the isocontours of Fig. 19.

the outer coma can be reliably traced back to surface features. The answer depends upon the opinion one has concerning the origin of these structures:

- If they come from very fine dust ($a_s \ll 0.1\ \mu m$) emitted by the nucleus—and which comoves with the gas far out—or from primary molecules emitted from the nucleus, then, unfortunately, we cannot answer at all the question at the present time. For such a purpose, we should introduce the localized emission of a minority molecule (or of fine, *collisional*, dust), i.e., develop a two-gas model. This is much more difficult than developing a two dust–fluid model, and has not yet been undertaken. The present results seem sufficient to deter one also from speculating without computing on such a matter.
- If they come from heavier dust ($0.01 \leq a_s \leq 100\ \mu m$), then it would seem that the answer is that they are absolutely *not* trivial tracers of the nucleus production map.

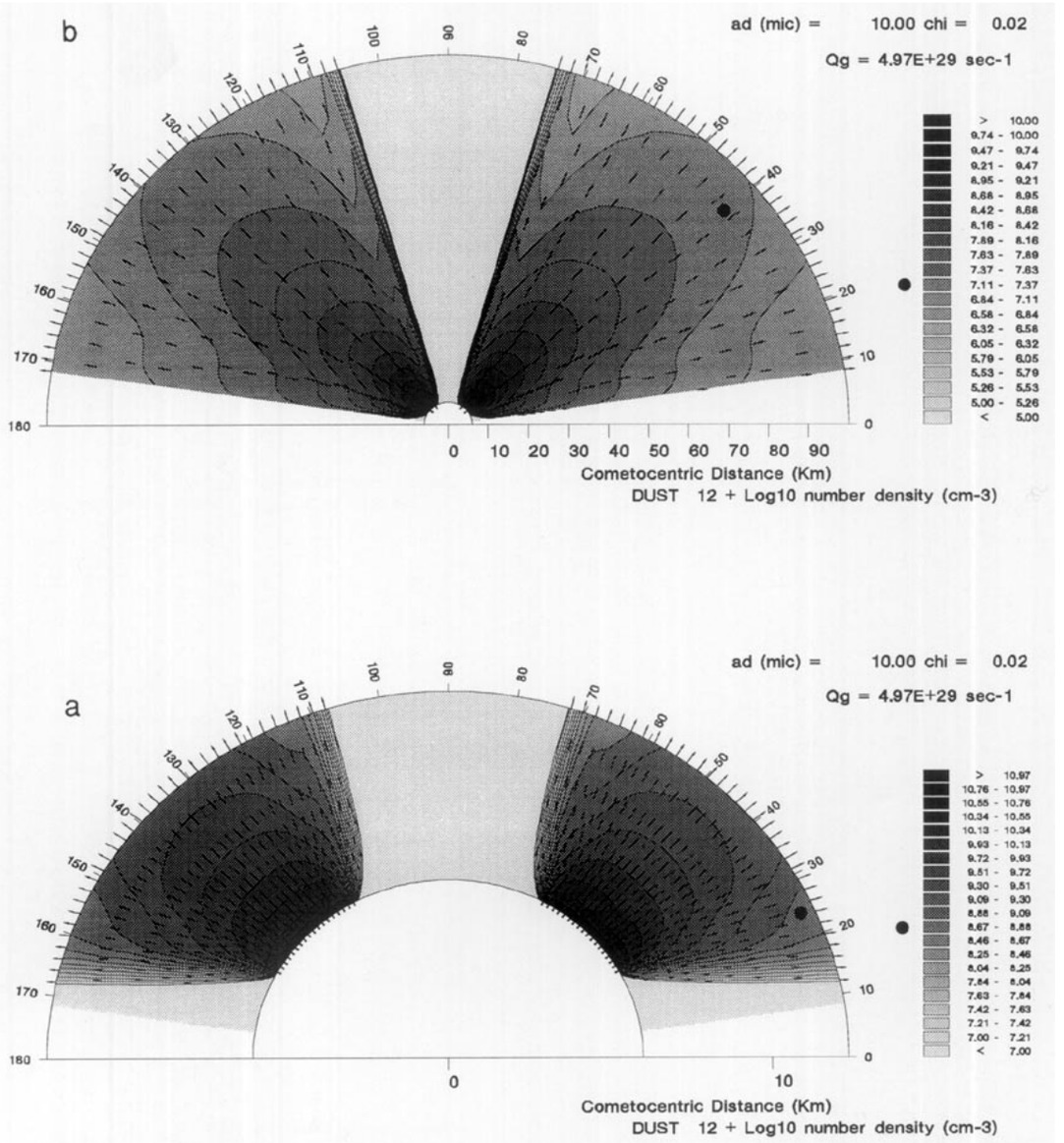

FIG. 21. Dust number density isocontours (cm^{-3}) and flow velocity for the same problem as in Figs. 18–20. Only the dust emanating from the left and from the right active areas is shown. By comparison with Figs. 14, 17, and 20, one can see the distortions due to the presence of the central active region. Superposition of the present isocontours and of those of Fig. 20 explains the structure of the isocontours of Fig. 19.

6.2. *On the Interpretation of Coma Dust Patterns*

Very fine dust follows the gas far out; therefore, we should expect its morphology to resemble that of the gas, i.e., this dust should not be a simple tracer of the surface production morphology. Intermediate size dust (1–10 μm) uncouples faster from the gas: it seems, as a preliminary guess, that its distribution outlines both the vertical of the active regions and the shock interfaces between these regions. We suspect that very heavy dust (mm size) will

FIG. 22. False-colour gas (top) and dust (bottom) isodensity contours in a coma formed by the interaction of three identical dusty gas jets. The left panels correspond to the case of a faint comet dominated by fine dust (parameters as n K90); the right panels correspond to a Halley-like comet dominated by intermediate-size dust (parameters given in Table III).

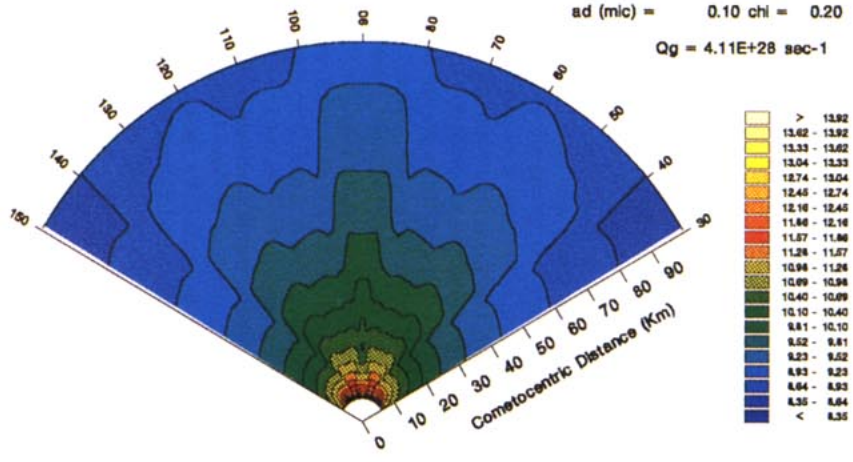
ad (mic) = 0.10 chi = 0.20
Qg = 4.11E+28 sec-1
Cometocentric Distance (Km)
ds_3x & ds_3xcon Thu Feb 9 15:00:39 1995 GAS Log10 number density (cm-3)

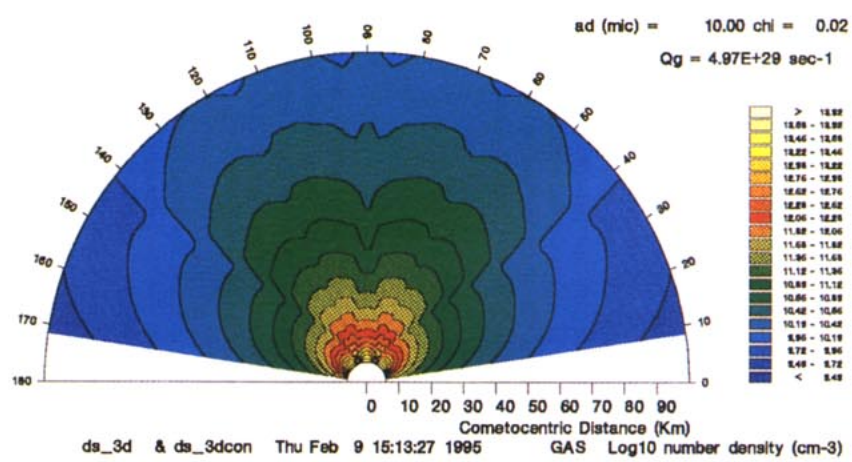
ad (mic) = 10.00 chi = 0.02
Qg = 4.97E+29 sec-1
Cometocentric Distance (Km)
ds_3d & ds_3dcon Thu Feb 9 15:13:27 1995 GAS Log10 number density (cm-3)

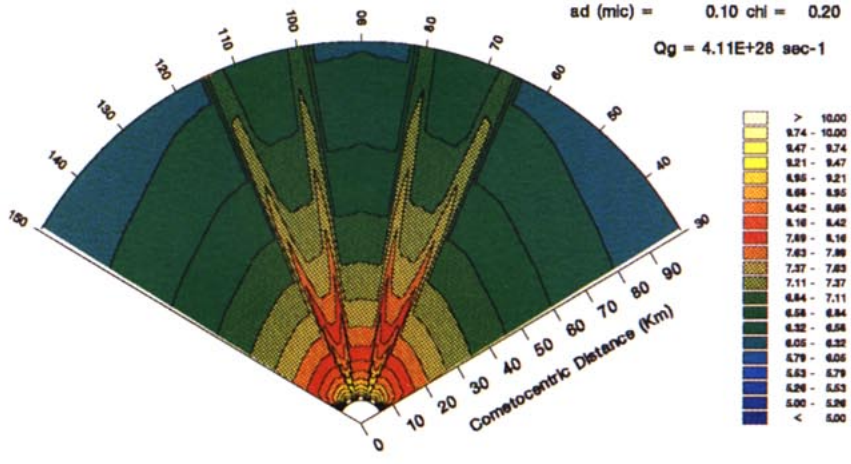
ad (mic) = 0.10 chi = 0.20
Qg = 4.11E+28 sec-1
Cometocentric Distance (Km)
ds_3x & ds_3xcon Thu Feb 9 15:06:35 1995 DUST 6 + Log10 number density (cm-3)

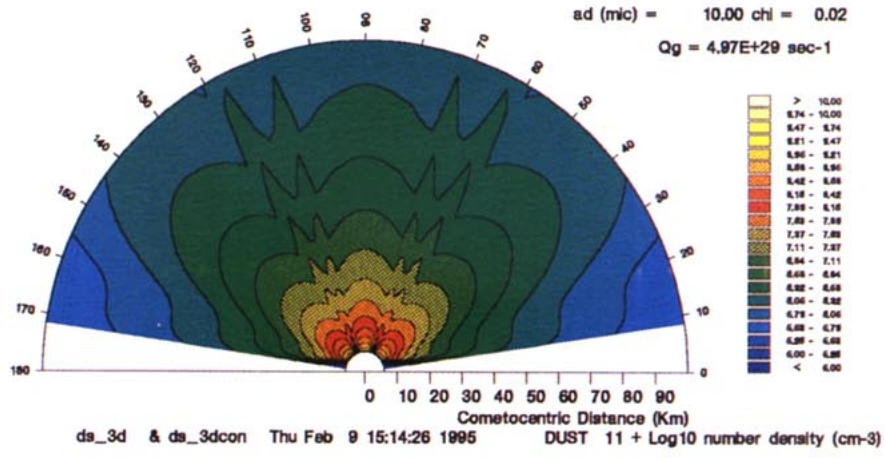
ad (mic) = 10.00 chi = 0.02
Qg = 4.97E+29 sec-1
Cometocentric Distance (Km)
ds_3d & ds_3dcon Thu Feb 9 15:14:26 1995 DUST 11 + Log10 number density (cm-3)

be more simply related to the active regions (at least, ignoring the nucleus rotation). However, the dust distribution is so sensitive to the details of the production (e.g., angular distance between regions) that a comprehensive set of simulations is needed before one can bring about firm conclusions concerning what may and may not be extracted from dust observations. This remark must be kept in mind when evaluating past (Keller *et al.* 1987) or future (Rosetta) interpretations of images of the immediate vicinity of a cometary nucleus. In fact, as already mentioned, the interpretation of images is further complicated by the need to sum over dust size and over line-of-sight.

As far as future in situ dust detections are concerned, future systematic studies will reveal which dust size (presumably very large) is more suited for a tentative nucleus mapping. On the other hand, in-situ dust detections may also be aimed at inferring the nucleus composition. In this respect, the present results demonstrate that the relative composition in solids of the active areas of a nucleus will be extremely difficult to reconstruct, to the extent that mass-dependent differential dispersion is at play.

6.3. *Limits of the Present Method*

These limits are set by the use of the inviscid assumption for the gas, of the fluid treatment for the dust, and by the crudeness of the physical model. The latter point is commented on in detail in Appendix A. Here, we wish to comment on the two first points.

In an inviscid flow, the local gas mfp $\Lambda(r)$ must be much smaller than the characteristic gas density variation scale $\mathcal{L}$. To evaluate Λ on the basis of known expressions (Crifo 1989), one has to assume a reasonable gas temperature (100 K) *instead of* the unphysical low values which follow from the neglect of recondensation. Considering that, away from the shocks and from the nucleus surface, $\mathcal{L} \approx r/2$, then one obtains $\Lambda/\mathcal{L} < \Lambda(r_m)/(r_m/2) \leq 0.04$.

Near the nucleus surface, however, details comparable to the numerical cell radial size Δr appear: away from the active area, one can obtain $\Lambda(r_0)/\Delta r(0) \simeq 1$, which means that the flow in *rarefied* regions adjacent to the surface *cannot be treated rigorously* by the present approach. If such regions were considered of great interest, it would be necessary to implement a full Navier–Stokes formalism (Crifo 1991), as was done in (Kitamura 1986); however, as discussed in Appendix A, for many other reasons the present treatment of the immediate vicinity of the surface is inadequate anyhow.

As far as dust is concerned, the computed dust m.i.d. never exceeds a few centimeters (see Figs. 4, 8, 10, 12, 14, 16, 19), thus is everywhere smaller than the local gas mfp; therefore, wherever the solutions hold for the gas, they also hold for the dust.

APPENDIX A

In the following, we discuss the relevance of the physical assumptions used in K90 and in the present computations. In first place, it must be recognized that assumptions of similar nature are commonplace in cometary gasdynamic publications. In our opinion, however, this is not a sufficient justification for not outlining the limitations of the results significance that follows from the nature of these assumptions. What the present, as well as the prior Kitamura, results show is the inadequacy of simple-minded analysis of coma flow patterns. However, as we argue below, it would be abusive as well to use these results to draw unequivocal conclusions concerning the origin of observed coma gas and dust patterns. At the present time, this seems to lie out of existing models' reach.

Dust Description

A realistic description of cometary dust implies consideration of a very broad dust size spectrum (McDonnell *et al.* 1991), and of a satisfactory optical model for the grains. This is not done here. For that reason, we do not make any discussion here on topics such as the near-nucleus coma dust brightness distribution, which absolutely requires such improvements.

A correct dust description is also requested for a realistic assessment of the gas–dust interactions. However, one can show that *for this purpose* it is sufficient to represent a P/Halley-like dust distribution by a *two-component* dust model with slightly differing $a_s \simeq 10$ μm, $\tilde{\rho}_s \simeq 4$ g cm^{-3}, $\chi \simeq 0.03$, and free-space temperatures $\simeq$300 K (Crifo 1987). Kitamura used a smaller a_s, a higher temperature and a much higher χ, which most likely *overestimates* the magnitude of the gas–dust interaction. Our revised single size dust parameters are reasonably close to the requested representation.

Initial Boundary Conditions

In first place, a comment on the significance of the initial radial distance r_0 is necessary: Eq. (1) implies inviscid gas flow; this is equivalent to saying that the gas distribution function is a strict Maxwellian. This however is never the case close to a gas/solid interface (with dimensions much larger than the mfp). It can be shown that, in the vicinity of such a surface, there exists a region ("boundary layer") with extent of the order of 10 mfp where the flow has special properties. Therefore, r_0 should be understood as being *away from the nucleus surface by about 10 mfp (here, a few meters)*. This seems to be a small distance; nonetheless both the gas and the fine dust parameters probably vary considerably across it. If one specifies a given process for the gas and dust production (e.g., dusty ice sublimation), it becomes possible to model quantitatively the boundary layer, solving the so-called Kramers problem. The case of pure ice sublimation is treated, for instance in Crifo (1991).

Here, as in K90, the Kramers problem is not treated, which amounts to assuming that the gas parameters at r_0 and at the surface coincide. This can be justified by the fact that one does not know for sure which process operates in real comets; pure ice sublimation is merely an assumption, not very likely in a natural medum; furthermore, it is not unreasonable to assume that the surface of a nucleus has corrugations on a scale of meters or even more. In which case the problem becomes untractable, because it is not any more *local*. Thus, there is considerable uncertainty concerning what realistic values of the gas and dust initial (ρ, $\mathbf{V}$, and T) may be.

In this study, these values were derived by he procedure of Appendix B.

In the future, it will be necessary to consider a choice of alternative

active area physical schemes and to treat correctly the surface/gas interface problem.

A similar uncertainty concerns the boundary conditions to be used on the inactive nucleus surface. It has been shown in (Kitamura 1987) that the assumption of slip-wall flow on the nucleus outside of the active areas significantly heats the gas.

Source-Sink Terms

As shown in Crifo (1991), the leading nonadiabatic effect close to the surface is the gas–dust interaction; shortly, it yields to water recondensation.

We have discussed above the problem of the gas–dust interaction.

Water recondensation in water jets is a well understood process (e.g., Itkin *et al.* 1991, Delale *et al.* 1993, Schnerr 1993). It has been studied for P/Halley flyby conditions in spherical geometry (Crifo 1990 and 1992).

The most visible consequence of the neglect of H_2O recondensation is the computation of totally irrealistic low gas temperatures. If a realistic (low temperature) chemical network is introduced in the model, it immediately predicts a partial recondensation of the gas strong enough to buffer the temperature in the 100 K region.

Here, we are interested in guessing to what extent the recondensation would alter the flow patterns of gas and dust. From the results of Crifo (1990 and 1992), one expects recondensation to set in about 0.1 km from the active area surface. The pressure increase due to the effect will affect the gas flow pattern (Delale *et al.* 1993, Schnerr 1993), but it is not possible to say more about it without quantitative modeling. One important point, however, is that it may only complicate the solution, but not make it simpler: the "rare gas" shock waves identified here will persist, with possibly superimposed new shock structures.

Compared to the omission of recondensation, the neglect of the other gas energy source-loss terms is somewhat inconsequential: the radiative cooling and photochemical heating are not dominant in the innermost coma, and their omission here is of secondary importance. However, this also forbids the use of the present model at distances much in excess of 100 km (P/Halley case).

APPENDIX B

Following the Kitamura (1986) approach, to determine the value of velocity immediately over the nucleus surface we need only the derivative of the velocity with respect to the radial coordinate r, because in the immediate vicinity of the surface the flow is nearly a one-dimensional radial flow from the surface. Thus to find dW/dr it is reasonable to suppose that all partial differentials with respect to angular variables vanish. In addition, as in Kitamura, we omit the derivative with respect to time; i.e., the solution is stationary. With this in mind, after some manipulations one can obtain the momentum equation for such a stationary spherically symmetric flow,

$$\frac{dW}{dr} = -\frac{1}{(1-M^2)}\left[\frac{2W}{r} + \frac{W\tilde{f}}{P} - \frac{(\gamma-1)f_h}{\gamma P}\right], \tag{B.1}$$

where W is the radial velocity, $\tilde{\mathbf{f}} \equiv (f_u, f_v, f_w)$, and f_u, f_v, f_w, f_h are the source-sink terms defined in Eq. (2.2).

In the following, we wish to use Eq. (B.1) for finding the gas velocity over the nucleus surface at each time $t = t^{n+1}$. For this purpose, we approximate dW/dr in each computational cell adjacent to the surface by performing in (B.1) the substitutions

$$\frac{dW}{dr} \to \frac{W^n_{1/2} - \hat{W}^{n+1}_*}{r_{1/2} - r_*}; \quad M \to \left[\frac{\mathbf{W}\cdot\mathbf{n}}{c_0}\right]^n_*; \quad W \to [(\mathbf{W}\cdot\mathbf{n})]^n_*; \quad P \to P^n_*$$

$$\tilde{f} \to [(\tilde{\mathbf{f}}\cdot\mathbf{n})]^n_{1/2}; \quad f_h \to [\tilde{f}]^n_{1/2}; \quad W^n_{1/2} \equiv (\mathbf{W}\cdot\mathbf{n})^n_{1/2}, \tag{B.2}$$

where $\hat{W}$ is the preliminary (unknown) value of the velocity, the subscript "1/2" relates to the center of the cells adjacent to the nucleus surface, the subscript "*" corresponds to the center of those cell sides which coincide with the nucleus surface, and $\mathbf{n}$ is the unit vector normal to the surface.

The resulting finite-diffence equation is solved for $\hat{W}^{n+1}_*$, after what the required value $\mathbf{W}^{n+1}_*$ is obtained by

$$\mathbf{W}^{n+1}_* = \hat{\alpha}\,\hat{W}^{n+1}_*\mathbf{n} + (1-\hat{\alpha})\,\mathbf{W}^n_*, \tag{B.3}$$

where $\hat{\alpha}$ is assumed to be constant (coefficient of smoothness: in our calculations we used $\hat{\alpha} = 0.1$).

In fact, we begin to use the above procedure only after several computational steps ($\simeq$500). Before that, the gas velocity over the nucleus surface is assumed to be constant, at a value arbitrarily chosen but in such a way that the Mach number immediately over the surface be less than unity. This is necessary, because in the first computational steps the gradients of the parameters are too large and the immediate use of the described procedure gives rise to computational errors.

It should be emphasized that such a procedure does not reveal the real *time-dependent* behavior of the flow parameters, but gives only the correct final solution corresponding to stationary conditions.

APPENDIX C

Numerical Method

Cartesian coordinates are used exclusively throughout the method. Spherical coordinates are used in this paper only as an intermediate tool to define the (Cartesian) coordinates of the computational grid points. So, the present formalism is already suitable for future completely aspherical solutions.

The computational network is produced by dividing the computational region into six-sided cells. The corner points of the cell (i, j, k) are the intersections of the surfaces $r = r_j$, $r = r_{j+1}$, $\theta = \theta_i$, $\theta = \theta_{i+1}$, $\phi = \phi_k$, $\phi = \phi_{k+1}$, where the subscripted quantities are generated by constant dividing steps $\Delta\theta \equiv \theta_{i+1} - \theta_i$ and $\Delta\phi \equiv \phi_{k+1} - \phi_k$, but by variable steps $\Delta r_j \equiv r_{j+1} - r_j$. In the time-dependent case, one also uses unequal steps $\Delta t^n \equiv t^{n+1} - t^n$.

For the solutions shown, $\Delta\theta$ and $\Delta\phi$ are given in Table III. As to the radial steps Δr, they are set as follows: between r_0 and r_1, there are J_1 radial steps with size increasing in geometric progression with $q = 1.1$; for the values of J_1 given in Table III, the first radial step is equal to about 100 m. Test simulations have shown that the results are insensitive to a decrease in q.

For $r > r_1$ the length of the step is found from the Courant condition (thus, at r_m it is about 10 km).

C.1. Integration of the Gas Equations

It was found optimal to use as the vector of unknowns $\mathbf{\Omega} = (u, v, w, \rho, P)$ instead of $\mathbf{U}$. The trivial relation $\mathbf{U} = \mathcal{U}(\mathbf{\Omega})$ is used to pass from $\mathbf{U}$ to $\mathbf{\Omega}$, and vice-versa.

C.1.1. The time-asymptotic region ($r_0 < r < r_1$). The present method derives $\mathbf{\Omega}$ *at the centers* of all computational cells. This implies also

assessing the values at the centers of all cell *sides*, and at the middle of the time intervals. Mid-point coordinates in space and time are labeled by half-integer indexes (e.g., $i \pm 1/2$). Thus, the values at the center of the cell with opposite corners $(i-1, j-1, k-1)$ and (i, j, k) and at time t^n are labeled $\mathbf{\Omega}^n_{i-1/2,j-1/2,k-1/2}$. However, for better readability, we will use the following abbreviations: subscripts equal to $(i-1/2)$, or to $(j-1/2)$, or to $(k-1/2)$ will be omitted; thus, $\mathbf{\Omega}_{j+2}$ will be the short form of $\mathbf{\Omega}_{i-1/2,j+2,k-1/2}$.

The integration of the system consists of passing from $\mathbf{\Omega}^n$ to $\mathbf{\Omega}^{n+1}$. The integration of Eqs. (2.1) over the above-mentioned cell, and from $t = t^n$ to $t = t^{n+1}$ gives the following relation between $\mathbf{\Omega}^n$ and $\mathbf{\Omega}^{n+1}$,

$$\Delta\Gamma\mathcal{U}(\mathbf{\Omega}^{n+1}) = \Delta\Gamma\mathcal{U}(\mathbf{\Omega}^n) + \Delta t(\mathbf{\Pi}^{n+1/2}_{i-1} + \mathbf{\Pi}^{n+1/2}_{j-1} + \mathbf{\Pi}^{n+1/2}_{k-1} - \mathbf{\Pi}^{n+1/2}_{i} - \mathbf{\Pi}^{n+1/2}_{j} - \mathbf{\Pi}^{n+1/2}_{k} + \Delta\Gamma\mathbf{H}^{n+1/2}), \tag{C.1}$$

where $\Delta\Gamma$ is the volume of the cell, and where $\mathbf{\Pi}_\alpha$ is a five-component vector: each component Π^β_α ($\alpha = i, j, k$; $\beta = 1, 2, 3, 4, 5$) is the flux across the cell side (α) of the three-component xyz-space vector (E^β, F^β, G^β).

If Ω^n and the source terms $\mathbf{H}^{n+1/2}$ are known, to obtain $\mathbf{\Omega}^{n+1}$ requires an evaluation of the six $\mathbf{\Pi}$s, thus an assessment of $\mathbf{\Omega}^{n+1/2}$ at the centers of the six cell *sides*. Following usual a widespread second-order nonoscillating technique, this is not done by trivial linear interpolation between adjacent cell center points, but assuming only linear variation of $\mathbf{\Omega}$ as a function of each spatial coordinate *inside* each cell; in other words, *two* values are defined at each cell *side* center: one corresponding to by extrapolation "from the left," and the other "from the right." We will call Ω^n_{i-} and Ω^n_{i+} the values on both sides of the ith cell side (and similar meanings for the j, k subscripted quantities).

As a consequence of this flexibility, the determination of $\mathbf{\Omega}^{n+1}$ requires knowledge, not only of the values $\mathbf{\Omega}^n$, but also of the increments along each direction:

$$\Delta_i\mathbf{\Omega} \equiv \mathbf{\Omega}^n_{i-} - \mathbf{\Omega}^n_{(i-1)+}, \quad \Delta_j\mathbf{\Omega} \equiv \mathbf{\Omega}^n_{j-} - \mathbf{\Omega}^n_{(j-1)+}, \quad \Delta_k\mathbf{\Omega} \equiv \mathbf{\Omega}^n_{k-} - \mathbf{\Omega}^n_{(k-1)+}. \tag{C.2}$$

This determination is done in four successive steps:

STEP 1. Preliminary values $\Delta_i\mathbf{\Omega}$, $\Delta_j\mathbf{\Omega}$, $\Delta_k\mathbf{\Omega}$ are calculated for each cell by the simple relations

$$\Delta_i\tilde{\mathbf{\Omega}} = \frac{\mathbf{\Omega}^n_{i+1/2} - \mathbf{\Omega}^n_{i-3/2}}{2}, \quad \Delta_j\tilde{\mathbf{\Omega}} = \frac{\mathbf{\Omega}^n_{j+1/2} - \mathbf{\Omega}^n_{j-3/2}}{2}, \quad \Delta_k\tilde{\mathbf{\Omega}} = \frac{\mathbf{\Omega}^n_{k+1/2} - \mathbf{\Omega}^n_{k-3/2}}{2}. \tag{C.3}$$

These values are then corrected by the monotonizing algorithm

$$\Delta_i\mathbf{\Omega} = \text{minmod}\{\Delta_i\tilde{\mathbf{\Omega}}, 2(\mathbf{\Omega}^n_{i+1/2} - \mathbf{\Omega}^n_{i-1/2}) - \Delta_i\tilde{\mathbf{\Omega}}_{i+1/2}, 2(\mathbf{\Omega}^n_{i-1/2} - \mathbf{\Omega}^n_{i-3/2}) - \Delta_j\tilde{\mathbf{\Omega}}_{i-3/2}\} \tag{C.4}$$

(and similar ones for $i \to j, k$)—where the function minmod is defined by

$$\text{minmod}[a, b, c, \ldots] = \begin{cases} \min[|a|, |b|, |c|, \ldots].\text{sign}(a), & \text{if } \text{sign}(a) = \text{sign}(b) = \ldots \\ 0, & \text{otherwise.} \end{cases}$$

STEP 2. Preliminary values $\tilde{\mathbf{\Omega}}^{n+1}$ are computed by Eqs. (C.1) with

$$\tilde{\mathbf{\Omega}}^{n+1/2}_i = \mathbf{\Omega}^n + \Delta_i\mathbf{\Omega}/2, \tilde{\mathbf{\Omega}}^{n+1/2}_{i-1} = \mathbf{\Omega}^n - \Delta_i\mathbf{\Omega}/2 \tag{C.5}$$

(and similar relations for $i \to j, k$).

STEP 3. The values $\mathbf{\Omega}^{n+1/2}_i$, $\mathbf{\Omega}^{n+1/2}_j$, $\mathbf{\Omega}^{n+1/2}_k$ on the cell boundaries are computed on the basis of the classical Riemann problem solution, using the values of $\mathbf{\Omega}$ on both sides of each cell as the initial discontinuity:

$$\mathbf{\Omega}^{n+1/2}_{i-} = \frac{1}{2}(\tilde{\mathbf{\Omega}}^{n+1}_{i-1/2} + \mathbf{\Omega}^n_{i-1/2} + \Delta_i\mathbf{\Omega}_{i-1/2}),$$
$$\mathbf{\Omega}^{n+1/2}_{i+} = \frac{1}{2}(\tilde{\mathbf{\Omega}}^{n+1}_{i+1/2} + \mathbf{\Omega}^n_{i+1/2} - \Delta_i\mathbf{\Omega}_{i+1/2}) \tag{C.6}$$

(and similar expressions for $i \to j, k$).

STEP 4. Using the precedingly computed parameters on the cell boundaries, the final values $\mathbf{\Omega}^{n+1}$ are calculated.

To complete the description of the computation procedure, one must, finally, specify the algorithm used to define the time integration step: for a true time-dependent problem, i.e., in which the details of the evolution of the solution with time are of interest (not only the final state), one should use

$$\Delta t < \Delta t^c \equiv \min_{i,j,k}(\Delta t^c_{i-1/2,j-1/2,k-1/2}), \tag{C.7}$$

where $\Delta t^c_{i-1/2,j-1/2,k-1/2}$ is the local maximum step Δt allowed by the Courant stability condition, and where $\min_{i,j,k}$ is the minimum taken at a given time, over all the computational cells.

However, when solving a time-asymptotic problem, only the final state matters; thus, the local integration step $\Delta t^c_{i-1/2,j-1/2,k-1/2}$ can be used at each cell, to increase the convergence rate to the final (steady) solution.

The present method can be shown to belong to the family of UNO2 schemes (uniform second-order nonoscillatory schemes); schemes of this kind are capable of confining the shock structures within one or two cells, without oscillations: in other words, the shocks are accurately located, instead of spreading over many cells (Harten and Osher 1987).

C.1.2. The steady marching region ($r_1 < r < r_m$). In the outer subregion, a time-independent "marching" method is used: in this case, the time derivatives are eliminated from Eqs. (2.1) and (2.4), and integration is performed in the direction of increasing j. Exactly the same procedure is used as in C.1.1, except that now:

1. the distance ξ transverse to the surfaces j = constant (which are, here, spheres, but, in the future, will be complex surfaces) plays the role of t precedingly (here, $\xi \equiv r$);
2. the vector of unknowns, $\mathbf{\Omega}$ is computed at the centers of the two-dimensional cells lying on the surfaces j = constant: the corresponding values are of the form $\Omega^j_{i-1/2,k-1/2}$;
3. at step 3, a steady analog of the Riemann problem is solved;
4. here the solution at each step of the marching is of interest. Therefore, use is made of marching steps

$$\Delta\xi < \Delta\xi^c \equiv \min_{i,k}(\Delta\xi^c_{i-1/2,k-1/2}), \tag{C.8}$$

where $\Delta\xi^c_{i-1/2,k-1/2}$ is the local maximum step allowed by the Courant stability condition.

C.2. *Integration of the Dust Dynamic Equations*

To integrate the dust dynamic Eqs. (2.4), the same computational network as for gas dynamic Eqs. (2.1) is used *for each dust fluid*. The integration method for Eqs. (2.4) is also nearly the same as that described in the previous section. There are only minor differences described in the following.

First, because the initial value chosen for T_s coincides with the free-space value $(q_{abs} f_\odot / 4 q_{em} \sigma)^{1/4}$, T_s remains practically constant throughout the flow (see Fig. 6 in Crifo (1987)). Therefore, we use as vector of unknowns for a dust fluid the four-component vector $\hat{\mathbf{\Omega}}_s \equiv (u_s, v_s, w_s, \rho_s)$.

Second, because a dust fluid has no internal pressure, the Riemann problem has a simple solution, which consists of the superposition of two uniform fluxes from both sides of the initial discontinuity. Depending upon the direction of the velocities of both fluids with respect to the normal to one cell side, there are four different kinds of solution: no flux crosses the side, the "left" flux only crosses it, the "right" flux only crosses it, both fluxes cross it.

Finally, the particles interact with the gas strongly. In that case, the technique for approximating the rhs of Eqs. (2.1) and (2.4) becomes critical. Here, the use of an explicit approximation can lead to the necessity of carrying out the calculations with extremely small integration steps Δt to provide stability against fast-relaxation processes. Instead, we use successive approximations of the source terms and a sequence of integrations of Eqs. (2.1) and (2.4) when passing from the nth surface of the $(n + 1)$-th one. Two differing methods are used, depending upon the region of integration.

C.2.1. The time-asymptotic region. Equations (2.4) are integrated initially with the source term approximation

$$\hat{\mathbf{H}}_s^{n+1/2} = \alpha \hat{\mathbf{H}}_s^n + (1 - \alpha) \hat{\mathbf{H}}_s^{n+1}, \tag{C.9}$$

where α is a parameter $(0 < \alpha < 1/2)$ and where the $(\hat{\ })$ denotes four-component vectors. This implicit system is solved as follows: using Eqs. (3.2), (3.3), and (3.6), one can write $\hat{\mathbf{H}}_s^{n+1}$ as

$$\hat{\mathbf{H}}_s^{n+1} = \rho_s^{n+1} \beta_1 \begin{vmatrix} 0 \\ u - u_s^{n+1} \\ v - v_s^{n+1} \\ w - w_s^{n+1} \end{vmatrix}, \tag{C.10}$$

where u, v, w, β_1 are calculated from the gas and dust parameters at the nth point in time.

Then, the interaction parameters $\mathbf{f}^d$ and f_h^d are calculated and the gas dynamic Eqs. (2.1) are integrated.

C.2.2. The Marching method region. Here, the approximation used along the marching direction is important. For that reason, the passage from the nth surface to the $(n + 1)$-th one is done by two cycles.

The first cycle starts from the solution of the gas dynamic equations with the interaction parameters obtained from the previous calculation step. Then, the dust unknowns $\hat{\mathbf{\Omega}}_s$ are calculated from an integration of Eqs. (2.4) with the approximations (C.9) and (C.10).

Here, in contrast to the time-asymptotic method, the values u, v, w, β_1 are calculated using the previously obtained gas parameters at the $(n + 1)$-th surface and dust parameters at the nth surface. Then, the interaction parameters are computed and the first cycle is finished.

The second cycle is identical to the preceding one, except that (1) when the gas dynamic equations are integrated, the new values of the exchange parameters are used; (2) when the dust dynamic equations are integrated, the values of u, v, w, β_1 are calculated using final computed gas parameters and the dust parameters at the $(n + 1)$-th surface from the first cycle.

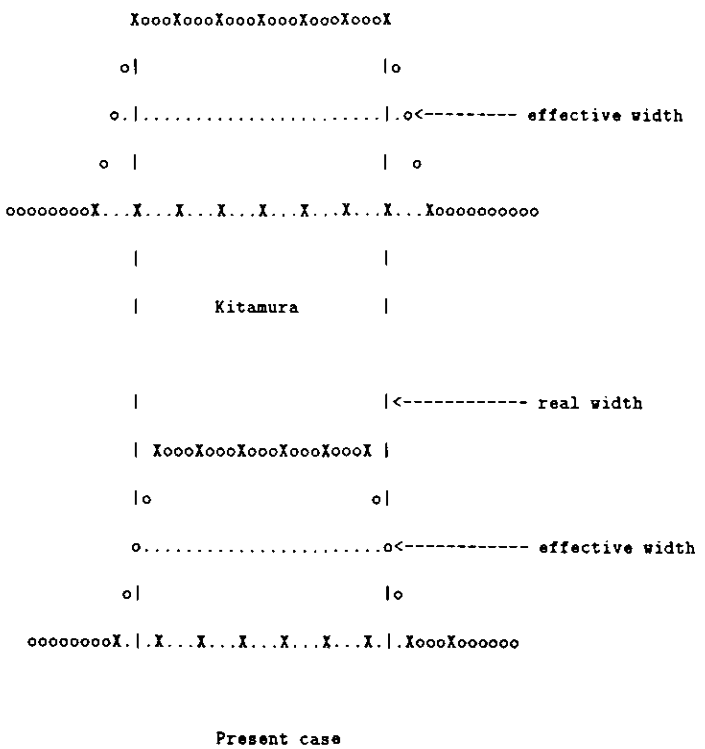

FIG. 23. The horizonal axis indicates distance onto the nucleus surface. The two vertical lines delineate the width of an active region; the crosses (X) show the computational points used by Kitamura (top) and here (bottom); the vertical scale refers to any parameter of the active region. One can see that the effective area of the region is overestimated by Kitamura.

APPENDIX D

The systematic difference in absolute densities found here and in K90 can be explained in the following way (Rodionov 1994). Mass flux conservation requires that, away from the surface, the fluid number density be proportional to the active region area, $\mathcal{A}$. Figure 23 sketches the initial profile of any fluid parameter (e.g., V) across an active region, and indicates the points at which values of V are computed: in K90, because the computational points are at corners of computational cells, there are points coincident with the edge of the region; in the present case, because the points are at cell centers, there are points on both sides of the edge, but not onto it. Thus, the *effective* width of the active region is, in the former case *in excess* of the correct value, while in the latter case *it is correct*. The excess factor by which $\mathcal{A}$ is evaluated in K90 is $[(N + 1)/N][(M + 1)/M]$, where M and N are the numbers of cells along the two active region widths. With $M = 5$ and $N = 6$, this is a factor $\simeq 1.4$: thus, the densities computed by Kitamura are about 40% too large.

ACKNOWLEDGMENTS

This work was supported by CNRS/INSU an CNES grants; one of us (A.V.R.) has benefited from a French MESR Fellowship. Support

received from the French Embassy in Moscow is also appreciated. Mrs. F. Bougnet and J. C. Lebrun are thanked for their assistance in using various computer facilities. Dr. Y. Kitamura and Prof. T. I. Gombosi are thanked from providing additional information on their past work. Finally, the encouragements and criticisms from the three anonymous referees were found very helpful.

REFERENCES

CRIFO, J. F. 1987. Optical and hydrodynamic implications of Comet Halley dust size distribution. In *The Diversity and Similarity of Comets*, ESA SP 278, pp. 399–408.

CRIFO, J. F. 1988. Are cometary mass loss rates deduced from optical emissions reliable? In *Proc. Xth European Regional Meeting of the IAU*, Czechoslovak Academy of Sciences Astronomical Institute Publication 67, Vol. 2, pp. 59–65.

CRIFO, J. F. 1989. Inferences concerning water vapour viscosity and mean free path at low temperatures. *Astron. Astrophys.* **223,** 365–368.

CRIFO, J. F. 1990. Water clusters in the coma of Comet Halley, and their effect on the gas density, temperature and velocity. *Icarus* **84,** 414–446.

CRIFO, J. F. 1991. Hydrodynamic models of the collisional coma. In *Comets in the Post-Halley Era* (R. L. Newburn, Jr., *et al.*, Eds.), Vol. 2, pp. 937–989. Kluwer Academic, Dordrecht.

CRIFO, J. F. 1992. Cometary gas-phase chemistry, taking into account homogeneous and ion-induced water recondensation. *Astrophys. J.* **391,** 336–352.

CRIFO, J. F. 1994. Elements of cometary aeronomy. *Curr. Sci.* **66,** 7–8, 583–602.

CROVISIER, J. 1984. The water molecule in comets: Fluorescence mechanisms and thermodynamics of the inner coma. *Astron. Astrophys.* **130,** 361–372.

DELALE, CAN F., G. H. SCHNERR, AND J. ZIEREP 1993. Asymptotic solutions of transonic nozzle flows wth homogeneous nucleation. I. Subcritical flows, 2. Supercritical flows. *Phys. Fluids A* **5,** 2969–2995.

GOMBOSI, T. I. 1991. Multidimensional dusty gasdynamic models of inner cometary atmospheres. In *Comets in the Post-Halley Era* (R. L. Newburn and J. Rahe, Eds.), Vol. 2, pp. 991–1004. Kluwer Academic, Dordrecht.

GOMBOSI, T. I., T. E. CRAVENS, AND A. F. NAGY 1985. Time-dependent dusty gasdynamic flow near cometary nuclei. *Astrophys. J.* **293,** 328–341.

HARTEN, A., AND S. OSHER 1987. Uniformly high-order accurate nonoscillatory schemes I. *SIAM J. Numer. Anal.* **24**(2), 287–309.

ITKIN, A. L., E. G. KOLESNICHENKO, AND Y. E. GORBATCHEV 1991. Analysis of Experimental Data on Nucleation Kinetics using the Monomolecular Theory of Recondensation. A. Ioffe Technical Institute Preprint 1523, St. Petersburg (in Russian).

KELLER, H. U., and 21 coauthors 1987. Comet P/Halley's nucleus and its activity. *Astron Astrophys.* **187,** 807–823.

KITAMURA Y, 1986. Axisymmetric dusty gas jet in the inner coma of a comet. *Icarus* **66,** 241–257.

KITAMURA, Y. 1987. Axisymmetric dusty gas jet in the inner coma of a comet. II. The case of isolated jets. *Icarus* **72,** 555–567.

KITAMURA, Y. 1990. A numerical study of the interaction between two cometary jets: A possibility of shock formation in cometary atmospheres. *Icarus* **86,** 455–475.

KÖMLE, N., AND W. H. LP 1987. Anisotropic non-stationary gas flow dynamics in the coma of comet P/Halley. *Astron. Astrophys.* **187,** 405–410.

KÖRÖSMEZEY, A., AND T. I. GOMBOSI 1990. A time-dependent dusty-gas dynamic model of axisymmetric cometary jets. *Icarus* **84,** 118–153.

MCDONNELL, J. A. M., P. L. LAMY, AND G. S. PANKIEWICZ 1991. Physical properties of cometary dust. In *Comets in the Post-Halley Era* (R. L. Newburn and J. Rahe, Eds.), Vol. 2, pp. 1043–1074. Kluwer Academic, Dordrecht.

RODIONOV, A. V. 1987a. Monotonic scheme of the second order of approximation for continuous calculation of non-equilibrium flows. *USSR Comput. Math. and Math. Phys.* **27**(2), 175–180.

RODIONOV, A. V. 1987b. Methods of increasing the accuracy of Godunov's scheme. *USSR Comput. Math. and Math. Phys.* **27**(6), 164–169.

RODIONOV, A. V. 1995. Application of Godunov's method modifications to simulation of spatial multiphase jets ejected from cometary nuclei. *Astron. Vestn.*, in press. [In Russian]

SCHNERR, G. H. 1993. Transonic aerodynamics including strong effects from heat addition. *Computers Fluids* **22,** 103–116.